The faint counterparts of MAMBO mm sources near the NTT Deep Field

H. Dannerbauer[2], M. D. Lehnert[2], D. Lutz[2], L. Tacconi[2], F. Bertoldi[3], C. Carilli[4], R. Genzel[2,5] & K. M. Menten[3]

ABSTRACT

We discuss identifications for 18 sources from our MAMBO 1.2mm survey of the region surrounding the NTT Deep Field. We have obtained accurate positions from Very Large Array 1.4 GHz interferometry and in a few cases IRAM mm interferometry, and have also made deep BVRIzJK imaging at ESO. We find thirteen 1.2mm sources associated with optical/near-infrared objects in the magnitude range K=19.0 to 22.5, while five are blank fields at K>22. We argue from a comparison of optical/near-infrared photometric redshifts and radio/mm redshift estimates that two of the thirteen optical/near-infrared objects are likely foreground objects distinct from the dust sources, one of them possibly lensing the mm source. The median redshift of the radio-identified mm sources is ∼2.6 from the radio/mm estimator, and the median optical/near-infrared photometric redshifts for the objects with counterparts ∼2.1. This suggests that those radio-identified mm sources without optical/near-infrared counterparts tend to lie at higher redshifts than those with optical/near-infrared counterparts. Compared to published identifications of objects from 850μm surveys of similar depth, the median K and I magnitudes of our counterparts are roughly two magnitudes fainter and the dispersion of I-K colors is less. Real differences in the median redshifts, residual mis-identifications with bright objects, cosmic variance, and

---

[1]Based on observations collected at ESO (66.A-0268, 67.A-0249, 69.A-0539, 70.A-0518, 71.A-0584) at the VLA, and on observations carried out with the IRAM PdBI. IRAM is supported by INSU/CNRS (France), MPG (Germany) and IGN (Spain). The Very Large Array is a facility of the National Radio Astronomy Observatory, which is operated by Associated Universities Inc., under cooperative agreement with the National Science Foundation.

[2]Max-Planck-Institut für extraterrestrische Physik, Postfach 1312, D-85741 Garching, Germany

[3]Max-Planck-Institut für Radioastronomie, Auf dem Hügel 69, 53121 Bonn, Germany

[4]National Radio Astronomy Observatory, P.O. Box O, Socorro, NM 87801, U.S.A.

[5]Department of Physics, Le Conte Hall, University of California, Berkeley, CA 94720, U.S.A.

small number statistics are likely to contribute to this significant difference, which also affects redshift measurement strategies. Some of the counterparts are red in J-K ($\gtrsim$20%), but the contribution of such mm objects to the recently studied population of near-infrared selected (J_s-K_s>2.3) high redshift galaxies is only of the order a few percent. The recovery rate of MAMBO sources by pre-selection of optically faint radio sources is relatively low (∼25%), in contrast to some claims of a higher rate for SCUBA sources (∼70%). In addition to this difference, the MAMBO sources also appear significantly fainter (∼1.5 magnitudes in the I-band) than radio pre-selected SCUBA sources. We discuss basic properties of the near-infrared/(sub)mm/radio spectral energy distributions of our galaxies and of interferometrically identified submm sources from the literature. From a comparison with submm objects with CO-confirmed spectroscopic redshifts we argue that roughly two thirds of the (sub)mm galaxies are at z$\gtrsim$2.5. This fraction is probably larger when including sources without radio counterparts.

Subject headings: galaxies: formation — galaxies: high-redshift — galaxies: starburst — infrared: galaxies — submillimeter

1. Introduction

With the discovery of distant submm and mm galaxies in blank field surveys and cluster lens assisted surveys (see Blain et al. 2002, for a review and references), it was immediately recognized that this population holds important clues for the understanding of the formation and evolution of galaxies. A significant part of the cosmic submm background is produced by these objects that must be extremely luminous ($L_{IR} \sim 10^{12-13} L_\odot$) distant (z$\gtrsim$1) infrared galaxies powered by intense star formation and/or powerful AGN. X-ray data argue in most cases against (Compton-thin) AGN and in favor of intense star formation dominating their luminosity (e.g., Alexander et al. 2003). These high star formation rates (≈100-1000 $M_\odot$/yr) and the similarity of co-moving space densities of submm sources and local ellipticals suggest that they are likely indicating the formation of massive spheroids. This opens a direct route to locating the formation of spheroids between the two extremes of an early formation similar to the classical 'monolithic collapse', and a late formation in hierarchical merging. More specifically, properties and mass functions for these high redshift objects are robust tests for current hierarchical models of galaxy formation (Guiderdoni et al. 1998; Kauffmann et al. 1999; Somerville, Primack, & Faber 2001; Baugh et al. 2003). Indeed there is evidence (e.g., Genzel et al. 2003; Neri et al. 2003) that these models need some modification to reproduce the space densities of the massive high redshift submm galaxies and their quiescent phases

that must exist since their star formation rates and gas content suggest a duty cycle of the bright (sub)mm phase well below one.

Much of this promise will only fully come to fruition after a difficult process of identification and spectroscopic redshift determination. Based on optical spectroscopy, significant progress in the identification work was done by Chapman et al. (2003a) who presented 10 redshifts of radio identified counterparts of SCUBA galaxies. But still, less than a dozen optical/near-infrared redshifts for suggested counterparts have been confirmed by CO observations as the true redshift of the submm source (Frayer et al. 1998, 1999; Neri et al. 2003, Greve et al. in prep, and SMM02399-0314, Kneib in prep.). Accurate positions from radio or mm interferometry are available for just a few dozen non-radio-preselected submm galaxies (e.g., Downes et al. 1999; Smail et al. 2000; Eales et al. 2000; Gear et al. 2000; Lutz et al. 2001; Ivison et al. 2002; Ledlow et al. 2002; Webb et al. 2003a,b) and very few mm-selected galaxies (Bertoldi et al. 2000; Dannerbauer et al. 2002). These accurate positions are indispensable for reliable optical/near-infrared identifications since several possible optical/near-infrared counterparts are usually found in the several arc second radius error circles of the (sub)mm surveys. This identification step is the subject of the present work. Of the two interferometric identification methods in use for (sub)mm sources, mm interferometry has the advantage of directly and unambiguously locating the dust emission, but it is very time consuming with current instruments, with tens of hours typically needed for a single object in the small field of view. Because of the tight radio/far-infrared relation for star-forming galaxies (e.g., de Jong et al. 1985; Helou et al. 1985; Condon 1992), radio interferometry is the next best option, with the advantage of the large VLA primary beam covering one of the currently typical (sub)mm survey fields entirely. Of the brighter (sub)mm sources from present surveys, deep 1.4GHz VLA maps will detect all but the highest redshift ones (Carilli & Yun 1999, 2000a; Barger et al. 2000), and the risk of false associations of (sub)mm and radio sources is modest for the 1.4GHz source counts at the relevant flux levels of tens of μJy (e.g., Richards et al. 2000).

We are building on our mm survey (Bertoldi et al. 2003, in preparation) that uses the MAMBO array (Kreysa et al. 1998) at the IRAM 30m telescope to cover three fields, the Lockman Hole, Abell 2125, and a region centered on, but larger than the NTT Deep Field (NDF, Arnouts et al. 1999). This paper focuses on the NDF region. Dannerbauer et al. (2002, hereafter Paper I) have presented results for three of the brightest NDF mm sources using the IRAM Plateau de Bure mm interferometer (PdBI) and BVRIK imaging. We now increase to 18 the number of NDF mm sources with accurate positions by using our VLA interferometry, and introduce additional z- and J-band optical/near-infrared imaging obtained since publishing Paper I. We thus identify counterparts and start assembling optical to radio spectral energy distributions (SEDs) of the objects constraining their nature and

redshift. The improved statistics is the basis for a discussion of the properties of mm galaxies and their relation to, or differences from, the submm population. Throughout the paper we adopt the cosmological parameters H_0=70 km s^{-1} Mpc^{-1}, Ω_M=0.3, Ω_Λ=0.7.

2. Observations, Data Reduction and Results

The radio data play a key role in the identification presented in this paper. The NTT deep field was observed at 1.4 GHz with the Very Large Array (VLA) in April and May, 2001, for 15 hours in the B configuration (10 km maximum baseline). Standard wide field imaging mode was employed (50 MHz total bandwidth with two polarizations and 16 spectral channels). The source 3C 286 was used for absolute gain calibration and 1224+035 was used for phase and bandpass calibration. The data were also self-calibrated using sources in the NTT deep field itself. Images were synthesized and deconvolved using the wide field imaging capabilities in the AIPS task IMAGR, and the primary beam correction was applied to the final image. The full width at half maximum (FWHM) of the Gaussian CLEAN beam was $7'' \times 5''$ with a PA = 0°. The rms noise on the final image is between 13 and 15 μJy over the $15' \times 15'$ region covered by MAMBO. The variation of the rms noise of the map was not only caused by the usual beam attenuation and UV plane coverage, but was also due to residual calibration errors because of a relatively large number of bright sources (2 sources of $\gtrsim$ 60 mJy/beam) and one spatial grouping of fainter but still relatively bright sources to the northeast of the center of the map. These residual calibration errors manifested themselves as uneven noise in a series of stripes in the final map. About 1/3 of area of the final VLA map was affected by this striping. We describe in § 2.1 how this was dealt with in identifying radio counterparts to the MAMBO 1.2mm detections.

We use the BVRIK imaging of a field centered on the NDF that is described in Paper I. We have obtained additional z and J-band imaging in spring 2003. The z-band observations were carried out in 'service mode' on the nights of April 6 and 7, 2003 using the imaging spectrograph FORS2 on UT4 of the VLT. The data were taken as a sequence of dithered exposures with a net integration time of 1 hour each covering 4 separate pointings. The pointings were chosen such that a mosaic of the images taken at the 4 pointings covers the whole of the K-band field centered on the NDF. The images were processed in the standard way but were flat-fielded using images generated by masking out all objects with surface brightnesses outside 1 sigma of the background noise and then combined by taking the pixel median of all the frames without the images being aligned. This flat-field frame was then normalized to one and then divided into each z-band image. Conditions were photometric throughout the observations and the seeing was typically about 0.5 arc seconds. The

final calibration was determined through observations of the spectrophotometric standard LTT7987 (Hamuy et al. 1994) for the z-band filter. However, given the very sensitive red response of the FORS2 array, the z-band filter was calibrated by integrating the spectral energy distribution of LTT7987 (Hamuy et al. 1994) and of BD+17 4708 (Oke & Gunn 1983) which is the absolute flux calibrator for the Gunn-z filter (Schneider et al. 1983). In making these estimates, both the response of the CCD and the filter transmission (both of which are available on the ESO web pages) were considered. The average noise across the frame is such that the 3σ detection limits in a $2''$ diameter aperture is $z_{BD+174708}$=26.38. The absolute flux distribution of LTT7987 provides a direct calibration of the images in the AB-magnitude system which yields z_{AB}=$z_{BD+174708}$-0.30. J-band imaging was obtained with SOFI at the ESO NTT between March 14 and 16 2003, covering the same $13' \times 13'$ region as our K_s image of the NDF to a 3σ limiting magnitude for a $2''$ aperture of 24.0 in J on the Vega system. Data reduction followed similar steps as described in Paper I, with the photometric zero point in J based on 2MASS. We used common sources to bring these new data to the same astrometric system as described in Paper I, including the small correction described in Paper I from the USNO-A1 based optical/near-infrared astrometry of our optical/near-infrared data to the radio reference frame. All positions quoted here include this correction and are on the radio frame.

2.1. Association of MAMBO sources with radio sources

In order to obtain more accurate positions for the MAMBO sources through use of their radio continuum emission, we have searched the 1.4 GHz VLA data for peaks of at least $40\,\mu$Jy ($\sim 3\sigma$) in the region where the MAMBO sources are located, out to radii of about $10'$ from the phase center. Table 1 lists the MAMBO sources in the catalog as of early 2002 which have radio sources with peak positions less than $7''$ from the nominal MAMBO map position. This radius is more than half the FWHM of the MAMBO beam and will not exclude real associations even in case of slight systematic offsets. The table, like all our subsequent analysis, does not include the well-detected quasar BR1202-0725 which was driving the original selection of the public ESO NDF, and thus cannot be considered an unbiased representative of the mm galaxy population. A more complete description of the MAMBO data analysis will be given in Bertoldi et al. (2003, in preparation). At $5'' \times 7''$ resolution, our B configuration data do not put interesting constraints on the extent of the radio emission of the detected galaxies. Table 1 also lists the corrected Poissonian probability that an association is a chance coincidence, derived using the approach of Downes et al. (1986) which corrects the simple Poissonian probability of an observed association for the possibility of associations of different nature but similar probability. In deriving these probabilities we

adopt the raw counts of $\geq$40μJy peaks in the region of our VLA image covered by the MAMBO data, which are significantly above the true 1.4GHz source counts for a flux close to the detection limit. Using true radio source counts (e.g., Richards et al. 2000) would thus have underestimated the chance of a false association. The probabilities listed together with the fact that 42 sources from the original MAMBO list were searched for nearby radio peaks suggest that several of the associations may be chance. This statistical analysis, however, does not adequately consider that the excess of $\sim$40μJy peaks boosting the rate of chance coincidences is largely due to peaks in the VLA map that cluster in certain regions, due to uneven noise and striping because of residual calibration errors. Considering this enables us to identify those associations that are more likely to be spurious by inspection of the distribution of $\geq$40μJy peaks in the radio map. The quality of an associated radio source is indicated in Table 1, with 'uncertain' assigned to sources with an excess of similar brightness peaks near to the suggested radio source, and in particular with alignments of peaks due to striping. We also consider as uncertain radio peaks that do not remain above 40μJy in a radio image where larger scale variations are partially removed by subtracting a 20$''$ median smoothed version of the radio image, and two faint radio peaks near sources No. 10 and 25 that are only above 40μJy in this image to which we refer as the 'background-subtracted' image below. Of the identifications we consider 'good' below, all but source 13 are either above 4σ in the original radio map, or confirmed by PdBI mm interferometry.

Figure 1 displays the mm–radio offsets corresponding to the associations listed in Table 1. The dominance of real associations is clear. There were no indications for systematic offsets. The separations found are consistent with a typical MAMBO position error of about 3$''$, and confirm the radius of 7$''$ as a sensible choice for searching for associated radio sources. Overall, interferometric positions are available for 18 out of 42 sources in the NDF MAMBO map. We consider 11 of these 18 reliable, either through 'good' radio peaks or through direct PdBI mm interferometry (Paper I). Interestingly, the PdBI data confirm the reality of two of the more uncertain radio sources, increasing confidence in the rest of these objects. The remaining MAMBO sources without radio associations could be at high redshift (with corresponding radio fluxes below our detection limit), could be spurious mm sources or have MAMBO fluxes systematically overestimated because of the bias induced by noise in a population with steep number counts. Given the signal-to-noise ratios of the MAMBO detections all these explanations may contribute. For the purpose of this identification paper, we do not discuss further objects without an interferometric position. This induces a bias towards lower redshift and brighter objects.

2.2. Optical and near-infrared objects near the radio positions

Images of $25'' \times 25''$ size in BRzK for the MAMBO sources with interferometric position are shown in Figure 2. Table 2 lists the positions and BVRIzJK photometric data of optical/near-infrared objects that are close to the interferometric positions. The photometry is in $2''$ diameter apertures centered on the positions which are derived from a first step SExtractor (Bertin & Arnouts 1996) analysis of a noise-scaled co-addition of the BVRIzJK images. Wavelength-dependent morphology can lead to small offsets of the peaks in certain bands from these average positions (Fig. 2). We have verified the reality of objects in Table 2 that are fainter than the 10σ completeness limit and close to the detection limit by visual inspection of the images in the various bands. We have retained objects that are reliably detected individually in either B,z, or K, these images being particularly deep and including the extreme wavelengths first detecting blue or very red objects. For the measurements in the individual bands, we indicate in Table 2 cases where we consider the SExtractor aperture magnitudes more uncertain, since the object is only tentatively (indicated by '$\approx$') or not (indicated by '!') picked up by the eye in the visual inspection. For simplicity, we designate the optical/near-infrared objects with a combination of the short MAMBO number (Table 1) and a letter increasing with distance from the interferometric position. These letters are also indicated in Fig. 2. The short MAMBO numbers used in this paper are consistent with the NTT-MMnn numbers used by Eales et al. (2003) in their comparison of 850μm and 1.2mm fluxes of MAMBO sources. BzK color composites of the objects are shown in Fig. 3.

We have used the publicly available *hyperz* photometric redshift code (Bolzonella et al. 2000) to estimate redshifts from our seven band photometry. We have verified the *hyperz* results for our specific photometric dataset by comparison of photometric redshifts to spectroscopic redshifts for 63 objects between z_{spec}=0.07 and 1.69 in the NTT Deep Field and its surroundings, for which spectroscopic redshifts are available from our own projects in that region and from ESO Science Verification data (http://www.eso.org/science/ut2sv/NDFs_release.html). The dispersion $\sigma_{zspec-zphot}$ of 0.17 is satisfactory, with few gross outliers. No trend between the accuracy of our photometric redshift and the color (R-K) is seen. We note however that *hyperz* does not contain an observed SED of a ultra-luminous infrared galaxy (ULIRG; which the SED of a mm sources may be similar), although it does allow for a range of additional extinction to be added to the model which may approximate a SED similar to that seen in ULIRGs. We notice a systematic effect at z$\lesssim$1, in the sense that photometric redshifts tend to be overestimated for sources with z$\lesssim$0.3 and underestimated in objects with 0.7$\lesssim$z$\lesssim$1.0. This is similar to what is seen in Subaru Deep Field photometric redshifts obtained with *hyperz* (Kashikawa et al. 2003, their Fig. 1). These systematic effects as well as the dispersion of z_{spec}-z_{phot} suggest that for individual bright objects the 1σ errors from *hyperz* in Table 2 underestimate the real errors, but at a level where the photometric redshifts are still valuable

constraints for the suggested counterparts and for nearby objects.

2.3. Identification and notes on individual objects

This section gives a case-by-case discussion of the individual interferometrically located MAMBO sources and identifies the suggested optical/near-infrared counterparts. We consider as possible counterparts optical/NIR objects that are less than 2 times the interferometric positional error (Table 1) away from the interferometric position. Again, we have derived the corrected Poissonian probabilities for a chance coincidence computed according to Downes et al. (1986) and considering the search radius of twice the radio positional error. Table 2 lists these probabilities for the objects inside the 2σ search circle, adopting the K-band number counts of Totani et al. (2001b). Deriving probabilities this way ignores color information and thus implicitly assumes a similar color distribution of counterparts and field population. In reality the colors differ (§ 3), i.e. we are overestimating the probability of a particular object being a random coinciding member of the field population.

For convenience, salient properties of the counterparts are collected in Table 3, full color information can be extracted from Table 1. Redshifts from the radio/submm spectral index are based on the flux densities from Table 1 and the relation of Carilli & Yun (2000b). These redshifts are subject to the applicability of the far-infrared SEDs used to calibrate this relation, and may be overestimated if cool luminous infrared galaxies (e.g. Chapman et al. 2002b) are prominent in the (sub)mm population. The possibility of 'cool' galaxies is also intimately related to the role of lensing in the identification of optical/near-infrared counterparts of submm sources (Blain et al. 1999; Chapman et al. 2002c) – as long as the redshift of the dust source is not confirmed through CO lines, certain configurations could correspond either to a 'cool' low z dust source or a 'warm' high z dust source with a superposed lensing foreground object. Therefore, for several objects, we present arguments on the potential role of lensing by individual foreground galaxies. These are simple plausibility arguments based on the observed K magnitudes and photometric redshifts, using after K-correction the K-band Faber-Jackson relation of Pahre et al. (1998) to estimate the velocity dispersion and the isothermal sphere approximation (e.g., Peacock 1999, his eq. 4-14) to estimate the radius of the Einstein ring.

MMJ120507-0748.1 (No. 03, g(ood) radio source) The faint, red counterpart 03a coincides with the 88μJy radio source. A $\sim 1''$ NW/SE double peak morphology for 3a may be indicated in the K_s image but is not certain. The optical/near-IR photometric redshift z$\sim$2.1 is consistent with the redshift estimate based on the radio-mm spectral index

(z_{CY} ∼2.4). The higher estimate z=4.25 from the submm/mm ratio (Eales et al. 2003) is uncertain and consistent with these lower values.

MMJ120508-0743.1 (No. 26, u(ncertain) radio source) A faint, uncertain radio source lies 4.6″ from the nominal MAMBO position. No optical/near-infrared counterpart coincides with this radio source.

MMJ120509-0740.0 (34, u) No optical/near-infrared counterpart is detected at the position of the faint, uncertain VLA counterpart. In the vicinity, an agglomeration of bright, normal galaxies is seen. The photometric redshifts of these objects (z_{phot} ≈0.4-0.5) are consistent with these galaxies perhaps being part of a group. At distances of >4.8″ from the interferometric position, lensing by these individual galaxies is unlikely. Similarly, a small group as such is not likely to produce a strong lensing effect (e.g., Hoekstra et al. 2001). Eales et al. (2003) fail to significantly detect at 850μm this object which is a 5σ 1.2mm source in the MAMBO map and was seen at similar flux (but only 2.2σ) in an independent short MAMBO on-off observation (Eales et al. 2003). The very low 850μm/1.2mm flux ratio as well as the non-detection of an optical/near-infrared counterpart may suggest a very high redshift.

MMJ120510-0747.0 (10, u) Near the nominal bolometer position lies a small separation (1.5″) galaxy pair of a fairly compact blue object (10a1) and a red (10a2) object. The interferometric position of the uncertain VLA source (seen only in the background-subtracted radio image) is about 2.4″ (1.9σ) north of 10a2 and slightly more distant from 10a1. It is thus marginally possible that one of the objects of this pair is the counterpart of the MAMBO source. Photometric redshifts suggest the blue object to be in the foreground rather than being physically associated with the red object, there are no secondary solutions for the photometric redshift which would put both at the same redshift. We tentatively identify the source with object 10a2. The high photometric redshift, consistent with the radio/mm estimate, is more uncertain than its nominal error given the faintness and the need to decompose the two components of 10a. At the observed K-band magnitude and estimated photometric redshift of 10a1, the estimated Einstein ring radius is only about 0.30″, making strong lensing of 10a2 at 1.5″ very unlikely. The same is true for other plausible redshifts. We note that 10a1 appears fairly compact and blue, spectroscopic observations to look for evidence of an AGN may be worthwhile. In case of a strong AGN its current photometric redshift estimate would be uncertain.

MMJ120516-0739.4 (36, g) This object has the strongest radio counterpart of a NDF 1.2mm source which coincides with a relatively bright and extremely red (R-K>6.0) source. The discrepancy between the redshift estimate from the radio/mm spectral index ($\sim$0.8) and the photometric redshift ($\sim$1.7) may suggest that the radio emission is boosted by an AGN.

MMJ120517-0743.1 (25, u) A faint radio counterpart is not seen in the original VLA image but in the background-subtracted version. It coincides with the position determined by mm interferometry (Dannerbauer et al. 2002, see their note added in proof). Recently, a faint K-band counterpart (22.5 magnitude) at the PdBI/VLA position was detected in ultra-deep imaging performed with ISAAC at the VLT (Lehnert et al. 2004, in preparation). Similarly, the new z band image indicates an extended source at the PdBI position with a maximum or companion to the southwest. In B, V and R very faint extended emission is suggested at the same position but only deeper imaging can reveal the reality of these structures. The photometric redshift is 2.91 in good agreement with the radio/mm redshift estimate and the mm/submm estimate of Eales et al. (2003).

MMJ120519-0749.5 (01, g) Among the 'blank field' sources not showing an optical/NIR counterpart within 2σ of the interferometric position, this is the blank field object with the strongest radio counterpart, that is also a secure radio source (72μJy). Eales et al. (2003) report a 4.3σ 850μm detection of this object, and infer a low 850μm/1.2mm flux ratio. This suggests a very high redshift which under the SED assumptions made is marginally consistent with the radio/mm redshift estimate. The objects a,d,e (Fig. 2) marginally detected by SExtractor seem to be due to noise or structure in the extended emission from the large foreground object and were not included in Table 2.

MMJ120520-0738.9 (39, g) The radio counterpart is the second strongest in our sample and coinciding to an ERO (R-K=5.2). In the K-band, it shows weak NW/SE extensions, with possible variations at shorter wavelengths. The high quality photometric redshift (1.32) and the radio/mm estimate agree well putting the object towards the low end of the redshift distribution of our mm sources. Object 39f, 7.6″ to the NW, has a very similar photometric redshift.

MMJ120522-0745.1 (18, g) The strong radio source which is 6″ SW from the nominal bolometer position coincides with an elongated moderate photometric redshift ERO (R-K=5.3), we here adopt it as counterpart of the MAMBO source noting the relatively large positional offset.

MMJ120524-0747.3 (08, u) Two faint and uncertain radio sources lie within the MAMBO beam. Both are blank fields in the optical/near-infrared. We adopt the μJy radio source closer to the nominal MAMBO position but consider the chance of a misidentification to be significant, both due to the radio sources being uncertain and the difficulty of deciding among them (Neri et al. 2003, cf. also the case of SMM09431+4700).

MMJ120526-0746.6 (13, g) A faint radio source from a good region of the VLA image coincides with an ERO (R-K=5.4). The K morphology appears distorted/curved. Both photometric redshift and radio/mm spectral index put the source at z≈2.5. This counterpart has very large J-K (and z-K) color, we will discuss this below in § 3.

MMJ120530-0741.6 (29, g) The interferometric position of the strong 85μJy radio source is in a group of three objects. Object 29a coincident with the radio position is at I-K=3.3 a very red object in the definition of Ivison et al. (2002). 1.5″ to the south-west there is a bluer source 29b, and 1.5″ to the north-west from 29a the extremely red object 29c (I-K>4.3). The photometric redshifts of the three objects are consistent with all being at z∼2.4, in reasonable agreement with the radio/mm estimate of ∼1.8. The three objects could be physically associated, with separations (for a redshift of ≈2) between about 13 and 23kpc. We nominally identify the MAMBO source with 29a but note that all three objects are part of a complex structure with strongly varying colors reflecting different obscurations, a unique object in our sample.

MMJ120530-0747.7 (07, u) A faint blue object coincides with a faint, uncertain radio source close to the edge of the search radius.[1] It is the only candidate counterpart which is not detected in the K-band and the bluest in our sample. The photometric redshift of 0.35 grossly differs from the radio/mm estimate (∼2.8), opening the possibility of the identification being incorrect and the object a foreground dwarf. The low mass of the relatively faint foreground object ($M_K \gtrsim -19$) makes a lensing effect less likely. The probability of ∼0.1 for a chance coincidence (in this case based on the B magnitude and the B counts of Pozzetti et al. 1998) is consistent with finding such a case in our sample.

MMJ120531-0748.1 (04, u) The identification in the optical/near-infrared is not obvious. The faint and uncertain radio source is 4.4″ from the nominal MAMBO position,

[1] At the chosen scaling when making the color images, the red channel appears noisier than the blue and green channels. Thus, we see enhanced "red" noise in the color image.

behind and 1.0″ from the center of an extended optical/near-infrared bright source (04a) with a photometric redshift estimate of 0.25. This is far below the radio/mm estimate. Galaxy-galaxy-lensing could hence play a significant role in MMJ120531-0748.1 — the radio position and the closest position on the estimated Einstein ring radius differ by less than 1σ of the radio positional error. The putative lensed object must be K$\gtrsim$18. The morphology could have similarity to SMMJ04431+0210 (Smail et al. 1999; Frayer et al. 2003), buth with a smaller separation making strong lensing more likely.

MMJ120534-0738.3 (42, g) This is the other of the two cases where two radio sources are detected within our search radius. The identification of the radio counterpart seems relatively clear, however, since a robust brighter radio source is only 2.1″ from the MAMBO position while the second is more distant (5.5″) and is both fainter and of uncertain reliability. We adopt the first one, which is located inside a group of three faint objects (42a-c) that are 1.3 - 2.0″ (1.6 to 3σ) from the radio position. An identification with 42a (z_{phot} =$1.52^{+0.24}_{-0.34}$) or 42b (z_{phot} =$2.83^{+0.67}_{-0.24}$) is possible, the radio/mm redshift estimate (z_{CY} ~2.1) is consistent with the photometric redshifts of either source. We adopt in the following an identification with the closest object 42a but consider an identification with b (or a blank field) possible. Source No. 42 appears extended in the MAMBO map, the peak flux (Table 1) thus underestimates the total flux. The source is in a border region between two K-band fields which may affect the quality of the K image and the photometric redshifts.

MMJ120539-0745.4 (16, g) While the radio counterpart is faint, its position is confirmed by the PdBI mm detection of Dannerbauer et al. (2002) which we adopt as best position. It is still a blank field in deeper images (K>22.7mag, Lehnert et al. 2004, in preparation).[2]

MMJ120545-0738.8 (40, u) A 40μJy uncertain radio source is located 3.9″ west of the nominal bolometer position. The faint object 40a is within 1.6σ of the radio positional error from the radio position. Directly at the MAMBO position and 4σ from the radio peak, however, a compact elliptical shaped extremely red object (40b) with a photometric redshift z=$1.52^{+1.24}_{-0.25}$ and a best-fitting burst-like SED is seen. An identification with this object may also be possible, its radio/mm index could still be consistent with the suggested photometric redshift range given the noise level of the VLA map. The observed radio peak

[2]The noise peaks in the K-band seen in the color image are due to overlaping regions between two separate pointings in our K-band mosaic.

would then be unrelated. Additional MAMBO on-off observations in winter 2001/2002 could not conclusively settle this ambiguity but showed the strongest signal at the position of the ERO. Only deeper radio interferometry or mm-interferometry can clarify this ambiguity, in the following we adopt an identification with the ERO which is another high J-K object.

MMJ120546-0741.5 (31, g) This source was discussed by Dannerbauer et al. (2002) and is a blank field at the depth of the images presented here. Lehnert et al. (2004, in preparation) detect a K-band counterpart (K_s=21.9mag) in VLT imaging. Eales et al. (2003) detect the source at 850μm and suggest a submm/mm redshift estimate consistent with the radio/mm estimate or with significantly higher redshifts.

2.4. Photometric redshifts vs. radio/mm redshift estimates

Figure 4 compares the photometric redshifts with the radio/mm redshift estimates. We consider this mostly a plausibility check given the uncertainties in both methods. The sources are often faint with relatively large photometric uncertainties in some of the band-passes (especially the optical ones), and the templates used in the photometric redshift estimates may not be fully appropriate for the likely ULIRG-like SEDs. The radio/mm redshift estimates are affected by the low significance of the radio and mm detections and the internal scatter of the relation for the radio/mm redshift estimate. It is reassuring that most sources are consistent with the main diagonal in this diagram, with few well defined exceptions. Two sources (07 and 04) are at low photometric redshift but high radio/mm estimate. We have argued above for the possibility of foreground objects in these two cases. One object (36) has a relatively low radio/mm estimate which could indicate AGN contribution but is still consistent with scatter in this relation. The optical 'blank fields' tend to have high radio/mm redshift estimates. This is clearly consistent with them being faint/obscured high redshift sources, but mis-identifications due to the relatively uncertain radio sources may also contribute.

3. Optical/near-infrared properties: very faint counterparts

The optical/NIR counterparts detected for the NDF mm sources are on average faint even compared to published values for submm galaxies. This is illustrated in Fig. 5 which shows the distributions of I and K band magnitudes and limits for our sample as well as for three samples of submm sources where these magnitudes are available for identifications obtained with the help of radio or mm interferometry. For consistency with our sample, we

did not consider from those papers the more unreliable identifications solely based on the bolometer survey positions. The first of these surveys is the SCUBA 8mJy survey (Scott et al. 2002; Ivison et al. 2002) which, for plausible assumptions on redshift and SED of the objects, should be roughly similar in depth to our data. The median submm flux of the radio-identified 8mJy sources is $S_{850\mu m}$ ∼8.3mJy, while the median mm flux of our radio-identified sources is $S_{1.2mm}$ ∼3.0mJy. This ratio ∼2.8 of 850μm and 1.2mm fluxes is consistent with z∼3 ULIRG-like SEDs and is borne out in studies of well-detected robust submm and mm sources (e.g., Hughes et al. 1998; Ivison et al. 1998; Gear et al. 2000; Ivison et al. 2000; Lutz et al. 2001). We have augmented data for the second set, the SCUBA cluster lens survey (Smail et al. 2002, and references therein), with two more objects behind one of their clusters detected by Cowie, Barger, & Kneib (2002) and discussed by Ledlow et al. (2002). For one of these we adopt the revised identification of Neri et al. (2003). Finally, we use magnitudes from the CUDSS survey, for radio identified objects in the 3h and 14h fields (Webb et al. 2003a,b) including the object studied by Gear et al. (2000). The latter two surveys differ more from our survey in strategy (cluster lens) or depth (CUDSS) but may still serve as comparisons.

As shown in Fig. 5, the NDF mm sources are significantly fainter both in K and in I. Taking the median of the observed magnitudes or limits, we find K∼21.5 and I∼25.5 for the mm objects versus K∼19.6 and I∼23.3 for the identifications from the 8mJy survey. The cluster lens and CUDSS objects have smaller statistics but show intermediate counterpart brightnesses (see also the recent deep SCLS imaging of Frayer et al. 2004, sometimes finding very faint counterparts). Eliminating all those NDF identifications based on radio sources that we considered more uncertain above does not change the values strongly - the median of the remaining objects is K∼20.9 and I∼24.9, i.e. the counterparts of the MAMBO sources are about 2 magnitudes fainter than those in the 8mJy 850μm survey. One major difference between the two populations is the absence in our sample of bright K∼18 counterparts, of which several are found for the 8mJy survey.[3] The trivial explanation of such a difference, our sample just representing much fainter members of the same population, is clearly inconsistent with the depths and areas of the various surveys. We also do not see a trend in our sample for bright mm sources being brighter in K, as possibly present in the SCUBA cluster lens survey (Smail et al. 2002).

[3]We note that different aperture sizes have been used in making this comparison. For example, Ivison et al. (2002) use a 3 arc second diameter aperture to estimate their fluxes intead of our 2 arc second apertures. In sources with complex extended morphologies or nearby objects, the larger apertures could lead to systematically brighter magnitudes. However, it seems unlikely that this alone could lead to an offset of 2 magnitudes.

3.1. Colors and the relation to field galaxies and the extremely red population

Another way to represent the optical/near-infrared properties is in the form of an I-K vs. K magnitude-color diagram as presented for SCUBA sources in Smail et al. (2002), Ivison et al. (2002), and Webb et al. (2003a,b). Again, we restrict our analysis (Fig. 6) to objects with interferometric positions. For comparison, the figure also includes the field galaxy population from our NDF data and the expected properties of objects with SEDs similar to local ULIRGs. For these, we have picked both an object that is red in the UV/optical (Arp 220) and a blue one (IRAS 22491-1808) from the objects studied in the UV by Trentham et al. (1999) and Goldader et al. (2002) and completed its SED with far-infrared data from Klaas et al. (2001) and large aperture optical/near-infrared data from elsewhere in the literature. The color-magnitude relation is then derived for these redshifted SED *shapes* but scaling the absolute flux to an observed flux of 5mJy at 1.2mm. The main results from this analysis are the following: First, the optical/near-infrared colors of (sub)mm galaxies scatter cover a wide range at a given magnitude (the 'diversity' of SCUBA galaxies, Ivison et al. 2000). Second, with few exceptions this range is within the envelope expected for the range of redshifted local ULIRG SEDs. These exceptions are from the 8mJy sample which generally has a surprisingly large scatter of I-K colors, larger than for the mm counterparts, and includes some very blue objects. In our sample we find only one object with a limit consistent with I-K<3.3 and one measurement I-K=3.33, while there are about half a dozen identifications in the 8mJy sample with objects at I-K<3.3, a color well in the range of the normal field population. Third, for K>19, the average (sub)mm source is redder in I-K than an average field galaxy of the same magnitude. This gives some support to the suggestion that nearby EROs are the most likely counterparts to SCUBA or MAMBO sources, but the dispersion in colors of both field galaxies and (sub)mm sources is too large to make this a robust criterion for identifications of individual submm sources without accurate positions. More specifically, the brightest (sub)mm counterparts (K<19) are statistically indistinguishable in I-K colors from the field population while (sub)mm counterparts are significantly redder at 19<K<21. It is difficult to quantify at this point how the trend continues at K>21 since observational limits in both K and I are significant for several of the samples involved. While the dispersion of I-K colors is larger for the 8mJy survey counterparts than for our objects we do not see a significant difference in the mean color at a given magnitude.

We compare the J-K colors which are available for our full sample with expectations for redshifted SEDs of ULIRGs. Fig. 7 shows the expected J-K colors as a function of redshift for a sample of six local ULIRGs, using their rest-frame UV to NIR SEDs assembled on the basis of the UV data of Trentham et al. (1999) and Goldader et al. (2002) and of large aperture optical/NIR photometry from the literature. For this type of SEDs, the J-K color is not a unique indicator of redshift, but excursions to large J-K colors can occur for redshifts

above 2 and red SEDs like that of Arp220. Like Fig. 6, this diagram shows the large variety of colors for local ULIRGs. The locations of the MAMBO sources spread from J-K$\sim$2, corresponding to intrinsically bluer SEDs or lower redshifts, to J-K>3.4 which is expected only for red Arp220-like SEDs and high redshifts. Again, the most likely interpretation is that the spread in the intrinsic optical/UV SEDs of mm galaxies is large, similar to the spread in local ULIRGs.

At least 5 of our 18 sources have ERO (I-K>4) counterparts. Given the long standing discussion about the contributions of passively evolving ellipticals and of dusty starbursts to this class, it is of interest to place our objects in this context. Fig. 8 shows an I-K vs. J-K color-color diagram proposed by Pozzetti & Mannucci (2000) to address this issue. Based on the dissimilarity between a 4000Å break and a reddened more smooth starburst continuum, this diagram is expected to separate the two categories for redshifts in the range of roughly 1 to 2. With the possible exception of MMJ12507-0748.1 (No. 03) the proposed mm and submm counterparts avoid the region of z$\sim$1-2 evolved populations, which might be found in case of false identifications of mm sources with such objects. It is not possible to draw the inverse conclusion from this diagram, i.e. to conclude that we are observing starbursts at z$\sim$1-2. The region populated by the (sub)mm sources is indicative of smooth spectra which are not very specific on redshift, or of spectra with a break between J and K. This caveat is particularly relevant since some (sub)mm objects are significantly fainter than the z$\sim$1-2 EROs for which this method was developed.

Recently, Franx et al. (2003) presented a technique to select optical-break galaxies at a redshift z>2 with the near-infrared filters J_s and K_s. van Dokkum et al. (2003) reported spectroscopic redshifts of a handful of such (J_s-K_s)>2.3 pre-selected galaxies, five of six indeed lying at redshifts higher than z>2 (z=2.4–3.5). Individual similar objects have been found in other surveys (e.g., Dickinson et al. 2000; Maihara et al. 2001; Totani et al. 2001a; Im et al. 2002, sometimes called 'HEROs'). We have probed for an overlap between this population and the MAMBO identifications. Franx et al. (2003) report a surface density of 3 ± 0.8 arcmin^{-2} for objects with J_s-K_s>2.3 and K_s <22.5. In our sample from a survey area of roughly 100 square arcmin we suggest 3 identifications with J-K>2.3, K<22 galaxies. Given several more J>24 limits, a few more might be found in deeper images to K=22.5 among the objects with current K>22 limits, and among the MAMBO sources without radio identification that are not discussed in this paper. It is thus fair to assume that the contribution of mm galaxies in the few mJy range to the population of luminous red galaxies as observed by Franx et al. (2003) is of the order one to a few percent. This small overlap is consistent with submm/mm followup for the four HEROs of Totani et al. (2001a), reporting very weak sub/mm signals (Coppin et al. 2002, and Andreani et al. in prep.). Also, only one of the six J_s-K_s>2.3 objects with spectroscopic redshifts reported by van Dokkum et al.

(2003) has a spectrum consistent with that of a dusty starburst. On the other hand, the fraction of red J-K sources (J_s-K_s>2.3 and K_s <22.5) in the mm population is significantly higher. Of our MAMBO sources with radio counterparts, at least 3 out of 18 (∼20%) are identified with red J-K sources. It may be higher, but the lack of deeper J-band data prevents us from estimating the colors of the faintest of the K-band counterparts. There might be an evolutionary connection beyond this small overlap, i.e. a contribution of mm galaxies in quiescent or post-active phases to the population of luminous red galaxies/HEROs.

3.2. Dependence on Radio Properties: Radio-Pre-Selection and Detection Limits

One of the major issues in our developing understanding of the nature of (sub)mm emitting galaxies at high redshift is how does the method of selection influence the properties of the sources? For example, targeted submm follow-up of optically faint radio sources (OFRS: $S_{1.4GHz} \geq 40\mu$Jy, I>25; Chapman et al. 2001) has been used as an efficient method to detect and study a significant 'radio pre-selected' fraction of the (sub)mm population. This is a particularly important comparison for our study. Because we have limited ourselves to a investigation of only those mm sources in the NDF with interferometric identifications, we might expect a radio-preselected sample to have similar properties. Indeed, the strength of the conclusions from such studies obviously depends on the amount of overlap with the population detected in unbiased 'blind' surveys (i.e., those not dependent of radio pre-selection), and on the nature of the biases induced by the OFRS selection. Both Barger et al. (2000) and Chapman et al. (2001), in comparing the submm detection efficiency of radio sources with that of blank field surveys, report a recovery rate of about 70% of bright (>5-6mJy) submm sources when targeting $S_{1.4GHz} \geq 40\mu$Jy radio sources with very faint near-infrared or optical counterparts (HK$'$ >20.5 or I>25, respectively). In contrast, only 10% of the refined 8mJy sample are reported to have an $S_{1.4GHz} \geq 40\mu$Jy, I>25 counterpart (Ivison et al. 2002). Using the same criteria, we recover 10 of 42 (about 25%) of the original NDF MAMBO list.

While the recovery fraction of optically faint radio identified sources presented here is similar to the low 8mJy recovery rate of Ivison et al. (2002) at first glance, a clear difference exists in the nature of the sources not matching the $S_{1.4GHz} \geq 40\mu$Jy, I>25 criteria. We find 7 to 8 (about 20%) optically bright (I<25) radio sources, while Ivison et al. (2002) find 12 of 30 optically bright sources (40%) in their refined sample with $S_{1.4GHz} \geq 40\mu$Jy radio counterparts. This is another manifestation of the clear difference in typical counterpart brightnesses between the NDF MAMBO sources and the 8mJy survey reported above. Ir-

respective of these differences, a large recovery rate by the radio pre-selection technique for faint optical sources is not supported by both 'blind' surveys.

Part of the difference between the suggested 70-75% recovery rates and the lower numbers found in the blind surveys may be simply due to reference integral counts of the complete submm population and due to small areas that we used in these surveys. The counts adopted by Barger et al. (2000) and Chapman et al. (2001) are more towards the low end of the spread of the count determinations summarized in Blain et al. (2002) and the number of sources in these field meeting their criteria was relatively small (for example, in Chapman et al. (2001), the recovery rate was determined based on 11 radio sources with submm detections and 2 sources without radio counterparts). In any case, a large recovery rate of the optically faint radio pre-selection is not ensured, and the selection effects are complex (see also Chapman et al. 2002a). While the radio detection will overall favor low redshift (Carilli & Yun 1999), optical faintness will prefer among those objects the higher redshifts ones. This is indeed suggested in our radio-identified sample where the mean redshift (approximated by the radio/mm indicator) is $< z >= 2.8 \pm 0.2$ for the I>25 objects compared to $< z >= 2.4 \pm 0.2$ overall.

While a comparison of the recovery rate of radio pre-selected sources with faint optical counterparts is interesting and instructive, perhaps a more robust comparison can be made with Chapman et al. (2003c). In Chapman et al. (2003c), the radio pre-selected sample is defined without imposing constraints on magnitudes of the optical/near-infrared counterparts to the radio sources, now finding noticeable numbers of optically brighter (I<25) radio-identified submm sources in contrast to the earlier radio-preselected studies. Overall, they recover about 70% of all submm sources which is formally higher than both the MAMBO source recovery rate for our survey and that of Ivison et al. (2002, which have recovery rates of ∼40% and ∼60% respectively). Similar to the differences we have found between our results and those of the 8 mJy SCUBA survey of Ivison et al. (2002), we also find a substantial difference between our results and the sources meeting our selection criteria of $S_{850\mu m}$ ∼8mJy and $S_{1.4GHz} \geq 40\mu$Jy in Chapman et al. (2003c). For the 10 sources in Chapman et al. (2003c) meeting these criteria, we find a median I-band magnitude of ≈24 with only 20% of the sources having I-band magnitudes fainter that I=25 (2 out of 10). Such a result is in stark contrast to our results with a median I-band magnitude of ∼25.5 and ∼80% of sources having I>25.

It is important to note that the differences in recovery rates and counterpart properties are not a direct consequence of the applied radio flux limits combined with strong trends with flux. Making a higher flux cut (40μJy as in our sample) in the radio detections of Ivison et al. (2002) only removes a small number of sources from their survey (3 or 4 depending

on how to treat a binary radio source, leaving a recovery rate of still ∼50%). Similarly, the majority of sources in the radio preselected samples of Barger et al. (2000), Chapman et al. (2001), and Chapman et al. (2003c) have $S_{1.4GHz} \geq 80\mu$Jy (well above their detection limit), changing the lower radio flux to our value thus has little effect .

4. Optical to radio SED constraints

We discuss the near-infrared (rest frame optical) to radio spectral energy distributions of our sources using an updated version of the diagram presented in Paper I, combining a spectral index between the K band and the submm and the well known radio/submm spectral index (Fig. 9). To be able to compare MAMBO and SCUBA sources, we estimate 850μm fluxes for those MAMBO sources where they have not been measured, by scaling the 1.2mm fluxes by a factor of 2.5 which is consistent with the median value of published ratios. This implicitly assumes that there is no major difference between the submm and mm populations. In Fig. 9, the MAMBO objects are also on average below the SCUBA ones, consistent with their optical/near-infrared faintness derived in the previous section.

Given the opposite trends in K corrections for the (sub)mm flux on one side and the radio and optical/NIR fluxes on the other side, redshifting a dusty galaxy SED will move the object from top left to lower right in this diagram. Such a trend is indeed indicated in the upper panel. The lower panel verifies and helps to visualize this expectation by plotting the loci for the redshifted SEDs of six local ULIRGs for which UV to radio SEDs are available. These clearly provide an indication of the scatter in the properties of the local population. In particular, significant offsets to the left are possible for objects with strong AGN, such as IRAS 19254-7245 with its reddened Type 2 AGN (Mirabel et al. 1991) and strong radio emission. It will be interesting to probe for AGN activity for the objects in the left (α(850μm,1.4GHz)$\lesssim$0.65) part of the diagram, indeed some of the objects there show evidence for AGN activity (LE850.12, Ivison et al. (2002), J02399-0134, Soucail et al. (1999)). For the radio/submm spectral index on the horizontal axis the dispersion for a larger sample is of the order 0.16 (Carilli & Yun 2000a), for the NIR/submm index of similar magnitude given the scatter arising from adopting different ULIRG SEDs (Fig. 3 of Paper I.). A similar scatter is observed in the high redshift (sub)mm population, shown by labeling in the top panel objects with CO-confirmed redshifts with the redshift value. Four of these six objects may also serve as an indication of a locus of z∼2.5 objects that is independent of the uncertain applicability of local templates. The average locus of these z=2.4 to 2.8 (mean z=2.6) objects is α(850μm,1.4GHz)=0.76 and α(2.2μm,850μm)=-0.99. Better statistics from on-going CO follow-up observations providing confirmed redshifts is

highly desirable to improve this calibration of Fig. 9. Although, the CO confirmed redshift may introduce an upward bias for this point if the successful optical redshift measurements on which they depend on correspond to brighter counterparts on average. Less bias should be present in the horizontal (radio/submm) direction. We find about two thirds of the MAMBO/SCUBA objects towards the 'high redshift' (z$\gtrsim$2.5) direction to the right of this point (43/69 at α(850μm,1.4GHz)>0.76). This is an underestimate, since the plot shows almost exclusively radio detected objects, thus missing roughly one-third to a half of the parent samples including the potentially highest redshift objects. Altogether, this indicates that the median redshift of 2.4 suggested for the bright SCUBA population from optical redshifts (Chapman et al. 2003a) is an underestimate of the median redshift of the complete population.

A conclusion drawn in Paper I from this type of diagram is that MAMBO and SCUBA sources are at high redshift and/or are at least as obscured as local ULIRGs. A technical factor affecting this reasoning is due to the unknown spatial structure of the objects. If the objects were very large and considering the effects of cosmological surface brightness dimming, the observed small structures (Fig. 2) may just reflect the central high surface brightness regions of more luminous extended objects that cannot be fully retrieved at realistic noise levels by just increasing aperture size. This would cause a tendency to underestimate the total near-infrared flux. There is evidence for some objects of that type in the (sub)mm population from near-IR imaging (e.g., Lockman 850.1, Lutz et al. 2001), and radio mapping (Ivison et al. 2002) finds some objects resolved by a 1.4$''$ beam. Examples of extended and complex morphologies are also seen in HST images of radio-preselected submm galaxies (Chapman et al. 2003b). For many other well studied (sub)mm sources the detected regions fit into 2$''$ apertures but this may be deceiving effects of surface brightness dimming if they are at very high redshift. Some estimate of the magnitude of the effect can be gained from comparison to the local ULIRG population. Half light radii have been estimated at several wavelengths, with median results of the order 5.3 kpc in U (Surace & Sanders 2000), 3 kpc in I (Zheng et al. 1999) and about 1.5 kpc in H and K (Colina et al. 2001; Tacconi et al. 2002). At redshifts around 3 an aperture of 2$''$ diameter spans about 15 kpc. Half light radii of $\sim$4 kpc in the rest frame V band (observed K band) would then mean no significant loss of light outside our aperture. This is only true as long as the structural analogy to local ULIRGs holds, of course, and a major fraction of light could be lost for objects more than a factor of 2 larger, especially if at z$\gtrsim$4. Such large objects would be placed too low in Fig. 9 by our measurements. This implies that the displacement of many SCUBA and MAMBO objects down-wards from the location of local ULIRGs could include an effect of large spatial extent as well as obscuration of the rest frame optical part of the SED. Testing such a scenario would require extremely deep K imaging. Size constraints at other wavelengths (optical,

mm, radio) will be useful as well, but for this question they will have to be interpreted with some caution considering the strong trends for local infrared galaxies, where half light radii decrease as wavelength increases.

5. What causes the difference between SCUBA and MAMBO populations?

The difference in brightness of about two magnitudes between typical MAMBO and SCUBA counterparts is a surprising result, given the selection of these objects at fairly similar wavelengths and on a part of the rest frame spectral energy distribution that does not show prominent breaks or features. We discuss in the following several potential contributors to this difference.

Given the faintness of the targets in comparison to instrumental sensitivities at *all* wavelengths, the identification process may still contain errors. For the NDF MAMBO sources, some of the near 3σ radio sources are clearly uncertain and may lead to uncertain identifications. We have argued above, however, that eliminating the uncertain sources as classified in § 2.1 does not change the magnitude distribution of the MAMBO counterparts significantly. For the SCUBA sources similar problems may be present at the limit of the radio data. In addition, there are by now examples where intensified identification efforts have rejected previously adopted bright counterparts and lead to a significant upward revision of the proposed counterpart magnitudes, the most notable being HDF850.1 (Hughes et al. 1998; Richards 1999; Downes et al. 1999; Dunlop et al. 2002), SMMJ00266+1708 (Frayer et al. 2000) and SMMJ09431+4700 (Neri et al. 2003). Taking away a few of the brightest or bluest 8mJy counterparts from Fig. 5 does not fully remove the difference to the MAMBO counterparts, though. Noting all these uncertainties we do not see any compelling evidence for systematic mis-identifications. Identification uncertainties are also related to the presence of 'complex' objects with several components, e.g., one of the mm galaxies discussed by Bertoldi et al. (2000). Ivison et al. (2002) emphasize the role of such objects in the 8mJy survey. Again, the example of SMMJ09431+4700 (Neri et al. 2003) where the submm and CO source H7 is $4''$ from the object H6 with a very similar (optical) redshift indicates that such grouping or clustering exists. In such cases, the (sub)mm source could relate to just one or to all of the components. We find only three such objects in our sample. For No. 10 we have preferred one component because of photometric redshift arguments. For objects 29 and 42 there is more uncertainty on whether to identify the source with one or several components, but even the sum of the components will not be a 'bright' counterpart.

Optical/near-infrared magnitude differences could also reflect a significant difference in the redshift distribution of the two populations. The effect in the optical/near-infrared

will obviously depend on the intrinsic SEDs, for ULIRG-like SED shapes and keeping the (sub)mm flux fixed a difference in median redshifts of the order Δz=1-2 may be necessary (Fig. 6). Chapman et al. (2003a) suggest a median redshift of 2.4 for bright submm galaxies from optical spectroscopy. Some of these optical redshifts still require confirmation by CO detections, and it is natural to assume that the optical redshifts are still biased towards the optically bright and low redshift end of the population. This assumption is supported by SED arguments (§ 4). Even at redshifts around or somewhat above 3, however, both SCUBA and MAMBO observations effectively sample the long wavelength side of the rest frame far-infared SED peak, unless the intrinsic dust temperatures were extremely cold. Evidence for both wavelengths sampling the long wavelength side is indeed present in many of the best studied SCUBA sources (e.g., Ivison et al. 1998; Downes et al. 1999; Gear et al. 2000; Ivison et al. 2000; Lutz et al. 2001). At such redshifts, it will be difficult to construct a redshift distribution that fully accounts for the observed differences. Redshift estimates for the SCUBA population from the radio/submm spectral index (Carilli & Yun 2000a), and from estimates trying to more fully include the rest-frame far-infrared part of the SED under the assumption of SEDs similar to local ULIRGs (Yun & Carilli 2002; Wiklind 2003; Aretxaga et al. 2003) indicate median redshifts in the range 2.5 to 3.5 with the possibility of a significant high redshift tail (Wiklind 2003; Aretxaga et al. 2003). However, it is important to note that such analysis suffer from possible template mismatches between high and low redshift sources and using an unrealistically narrow range of SED types and properties when making redshift estimates. For example, Aretxaga et al. (2003) may perhaps put undue weight on single templates by matching one template to each source to constrain the possible redshift range. This means that low redshift SEDs they have in their analysis must be good analogues for high redshift sources. In addition, a substantial number of higher redshift z>4 sources in the MAMBO population is also suggested by the 850μm/1.2mm ratios presented by Eales et al. (2003), albeit with large uncertainties due to the technical difficulties of the method. For the objects overlapping with our study (Nos. 1, 3, 16, 25, 31) their 850μm/1.2mm redshift estimates can be compared to the detection in various optical pass-bands - if they are at high redshift, these objects should be undetected dropouts in optical bands. With the possible exception of No.3 (best submm/mm estimate z$\sim$4.25 but a marginal detection in B) the results are consistent, and even for this object considering the uncertainties. In summary, while there may be a high redshift tail of the (sub)mm population preferentially sampled by MAMBO, we find it difficult to explain the magnitude differences by a bulk redshift difference. This view is consistent with Fig. 9 which does not only show the ‘diagonal’ offset between the two sets expected in such a case.

Because of the degeneracy of redshift and dust temperature in interpretations of the submm/radio spectral energy distributions (e.g. Blain et al. 2003), similar arguments can be

made with respect to a possible separation of the MAMBO and SCUBA populations by dust temperature, for example due to an evolutionary difference between MAMBO and SCUBA objects. One should note, however, the need for significant obscuration in the rest frame optical when invoking 'cool' rest-frame FIR SEDs (e.g., Paper I).

The results shown here indicate that there are real differences in the counterpart brightnesses and perhaps redshifts of the SCUBA and MAMBO populations. On the sole basis of the SED arguments presented it is difficult to robustly weight the contributions of real differences in redshifts and spectral energy distributions of the mm and submm selected populations to this difference, in comparison to caveats due to small sample statistics, cosmic variance, and identification difficulties. Significant progress in settling these issues will come from tests of proposed identifications with available optical redshifts through CO measurements (e.g., Neri et al. 2003), and from future direct submm/mm redshift measurements for the fainter part of the population, most likely through wide band searches for CO emission.

6. Conclusions

We have discussed optical/near-infrared identifications for those 18 of 42 sources in our MAMBO 1.2mm map of the NTT Deep Field region for which interferometric positions are available through a VLA 1.4GHz map and in three cases IRAM PdBI mm interferometry. In addition to being the basis for identifications, our deep BVRIzJK imaging allows the derivation of optical/near-infrared photometric redshifts for the counterparts and for nearby objects. In comparison with radio/submm redshift estimates, these photometric redshifts suggest that two of the optical/near-infrared sources close to interferometric positions are in the foreground, in one case likely lensing the background mm source. One strongly lensed object in this sample is consistent with expectations for the (sub)mm population (Blain et al. 1999; Chapman et al. 2002c). This leaves us with eleven detections of counterparts at magnitudes of K=19 to 22.5, and seven limits or blank fields with most limits at K>22. The I-K and J-K colors of the counterparts are consistent with redshifted SEDs similar to local ultra-luminous infrared galaxies, and likely with a similarly large spread of the rest frame UV/optical SED properties. The counterparts of mm sources contribute to the recently discussed population of J-K>2.3, K<22.5 high redshift galaxies, but only at the few percent level for the current mm survey depths. At least $\sim$20% of the MAMBO sources with radio counterparts have J-K>2.3 and K<22.5.

The counterparts to NDF mm sources are on average about 2 magnitudes fainter than counterparts presented for the 8mJy 850μm survey which is of similar depth and are similarly faint compared to radio pre-selected submm sources. Remaining mis-identifications, redshift

or temperature differences between the two populations, and small number statistics/cosmic variance all may contribute to this difference, at levels that are hard to quantify from currently available data. Our result reinforces the view that direct (e.g., wide band CO) spectroscopic redshifts may be necessary for a substantial fraction of the (sub)mm population which is very faint in the optical/near-infrared. From a comparison of near-infrared/submm/radio spectral indices with those of submm sources with CO-confirmed redshifts we suggest that the fraction of (sub)mm galaxies at $z>2.5$ is about two thirds for the interferometrically located ones and larger when adding the radio-undetected part of the population.

We would like to thank the staffs of ESO, IRAM, and VLA for their support with the data acquisition and reduction. We thank Andrew Baker for helpful discussions. We also acknowledge the contributions of the referee in clarifying a number of important points. This research has made use of the NASA/IPAC Extragalactic Database (NED) which is operated by the Jet Propulsion Laboratory, California Institute of Technology, under contract with the National Aeronautics and Space Administration.

REFERENCES

Alexander, D. M., Bauer, F. M., Brandt, W. N., Hornschemeier, A. E., Vignalli, C., Garmire, G. P., Schneider, D. P., Chartas, G., & Gallagher, S. C. 2003, AJ, 125, 383

Aretxaga I., Hughes, D., Chapin, E., Gaztañaga, E., Dunlop, J.S., Ivison, R.I. 2003, MNRAS, 342, 759

Arnouts, S., D'Odorico, S., Cristiani, S., Zaggia, S., Fontana, A., & Giallongo, E. 1999, A&A, 341, 641

Barger, A., Cowie, L.L., Richards, E.A. 2000, AJ, 119, 2092

Baugh, C.M., Benson, A.J., Cole, S., Frenk, C.S., Lacey, C. 2003, in: The Masses of Galaxies at Low and High Redshift, eds. R.Bender & A. Renzini (Berlin: Springer), p. 91

Bertin, E., Arnouts, S. 1996, A&AS, 117, 393

Bertoldi, F. et al. 2000, A&A, 360, 92

Blain, A.W., Möller, O., Maller, A. 1999, MNRAS, 303, 423

Blain, A., Smail,I., Ivison,R.J., Kneib,J.-P., Frayer,D.T. 2002, PhR, 369, 111

Blain, A., Barnard, V.E., Chapman, S.C. 2003, MNRAS, 338, 733

Bolzonella, M., Miralles, J.-M., Pello, R. 2000, A&A, 363, 467

Carilli, C.L., Yun, M.S. 1999, ApJ, 513, L13

Carilli, C.L., Yun, M.S. 2000a, ApJ, 530, 618

Carilli, C.L., Yun, M.S. 2000b, ApJ, 539, 1024

Chapman, S.C., Richards, E.A., Lewis, G.F., Wilson, G., Barger, A.J. 2001, ApJ, 548, L147

Chapman, S.C., Lewis, G.F., Scott, D., Borys, C., Richards, E. 2002a, ApJ, 570, 557

Chapman, S. C., Smail, I., Ivison, R. J., Helou, G., Dale, D. A., & Lagache, G. 2002b, ApJ, 573, 66

Chapman, S.C., Smail, I., Ivison, R.J., Blain, A.W. 2002c, MNRAS, 335, L17

Chapman, S.C., Blain, A.W., Ivison, R.J., Smail, I.R. 2003a, Nature, 422, 695

Chapman, S.C., Windhorst, R., Odewahn, S., Yan, H., Conselice, C. 2003b, ApJ, in press (astro-ph/0308197)

Chapman, S.C., et al. 2003c, ApJ, 585, 57

Colina, L., et al. 2001, ApJ, 563, 546

Condon, J.J. 1992, ARA&A, 30, 575

Coppin, K., et al. 2002, BAAS, 201, #06.19

Cowie, L.L., Barger, A.J., & Kneib, J.-P. 2002, AJ, 123, 2197

Dannerbauer, H., Lehnert, M.D., Lutz, D., Tacconi, L., Bertoldi, F., Carilli, C., Genzel, R., Menten, K. 2002, ApJ, 573, 473 (Paper I)

de Jong, T., Klein, U., Wielebinski, R., Wunderlich, E. 1985, A&A, 147, L6

Dickinson, M., et al. 2000, ApJ, 531, 624

Downes, A.J.B., Peacock, J.A., Savage, A., Carrie, D.R. 1986, MNRAS, 218, 31

Downes, D. et al. 1999, A&A, 347, 809

Dunlop, J.S., et al. 2002, MNRAS, submitted, astro-ph/0205480

Eales, S., Lilly, S., Webb, T., Dunne, L., Gear, W., Clements, D., Yun, M. 2000, ApJ, 120, 2244

Eales, S., Bertoldi, F., Ivison, R., Carilli, C., Dunne, L., & Owen, F. 2003, MNRAS, 344, 169

Frayer, D.T., Ivison, R.J., Scoville, N.Z., Yun, M., Evans, A.S., Smail, I., Blain, A.W., Kneib, J.-P. 1998, ApJ, 506, L7

Frayer, D.T., et al. 1999, ApJ, 514, L13

Frayer, D.T., Smail, I., Ivison, R.J., Scoville, N.Z. 2000, AJ, 120, 1668

Frayer, D. T., Armus, L., Scoville, N.Z., Blain, A.W., Reddy, N.A., Ivison, R.J., Smail, I. 2003, AJ, 126, 73

Frayer, D. T., Reddy, N. A., Armus, L., Blain, A. W., Scoville, N. Z., & Smail, I. 2004, AJ, in press (astro-ph/0310656)

Franx, M. et al. 2003, ApJ, 587, L79

Gear, W.K., Lilly, S. J., Stevens, J.A., Clements, D.L., Webb, T.M., Eales, S.A., & Dunne, L. 2000, MNRAS, 316, L51

Genzel, R., Baker, A.J., Tacconi, L.J., Lutz, D., Cox, P., Guilloteau, S., Omont, A. 2003, ApJ, 584, 633

Goldader, J.D., Meurer, G., Heckman T.M., Seibert M., Sanders, D.B., Calzetti, D. and Steidel C.C. 2002, ApJ, 568, 651

Guiderdoni, B., Hivon, E., Bouchet, F. R., & Maffei, B. 1998, MNRAS, 295, 877

Hamuy, M., Suntzeff, N. B., Heathcote, S. R., Walker, A. R., Gigoux, P., & Phillips, M. M. 1994, PASP, 106, 566

Helou, G., Soifer, B.T., Rowan-Robinson, M. 1985, ApJ, 298, L7

Hoekstra., H., et al. 2001 ApJ, 548, L5

Hughes, D. H. et al. 1998, Nature, 394, 241

Im, M., Yamada, T., Tanaka, T., Kajisawa, M. 2002, ApJ, 578, L19

Ivison, R.J., Smail, I., Le Borgne, J.-F., Blain, A.W., Kneib, J.-P., Bézecourt, J., Kerr, T.H., Davies, J.K. 1998, MNRAS, 298, 583

Ivison, R.J., Smail, I., Barger, A.J., Kneib, J.P., Blain, A.W., Owen, F.N., Kerr, T.H., & Cowie, L.L. 2000, MNRAS, 315, 209

Ivison, R.J., et al. 2002, MNRAS, 337, 1

Kashikawa, N., et al. 2003, AJ, 125, 53

Kauffmann, G., Colberg, J.M., Diaferio, A., White, S.D.M. 1999, MNRAS, 303, 188

Klaas, U. et al. 2001, A&A, 379, 823

Kreysa, E. et al. 1998, Proc. SPIE, 3357, 319

Ledlow, M.J., Smail, I., Owen, F.N., Keel, W.C., Ivison, R.J., Morrison, G.E. 2002, ApJ, 577, L79

Lutz, D. et al. 2001, A&A, 378, 70

Maihara, T., et al. 2001, PASJ, 53, 25

Mirabel, I.F., Lutz, D., Maza, J. 1991, A&A, 256, L19

Neri, R. et al. 2003, ApJ, 597, L113

Oke, J. B., & Gunn, J. E. 1983, ApJ, 266, 713

Pahre, M.A., Djorgovski, S.G., de Carvalho, R.R. 1998, AJ, 116, 1591

Pozzetti, L., Madau, P., Zamorani, G., Ferguson, H.C., Bruzual, G. 1998, MNRAS, 298, 1133

Peacock, J.A. 1999, Cosmological Physics (Cambridge: Cambridge University Press)

Persson, S.E., Murphy, D.C., Krzeminski, W., Roth, M., & Rieke, M.J. 1998, AJ, 116, 2475

Pozzetti, L. & Mannucci, F. 2000, MNRAS, 317, L17

Richards, E.A. 1999, ApJ, 513, L9

Richards, E.A. 2000, ApJ, 533, 611

Schneider, D. P., Gunn, J. E., Hoessel, J. G. 1983, ApJ, 264, 337

Scott, S.E. et al. 2002, MNRAS, 331, 817

Smail, I., Ivison, R.J., Kneib, J.-P., Cowie, L.L., Blain, A.W., Barger, A.J., Owen, F.N., Morrison, G., 1999, MNRAS, 308, 1061

Smail, I., Ivison, R.J., Owen, F.N., Blain, A.W., Kneib, J.P. 2000, ApJ, 528, 612

Smail, I., Ivison, R.J., Blain, A.W., Kneib J.-P. 2002, MNRAS, 331, 495

Somerville, R. S., Primack, J. R., & Faber, S. M. 2001, MNRAS, 320, 504

Soucail, G., Kneib, J.P., Bézecourt, J., Metcalfe, L., Altieri, B., Le Borgne, J.F. 1999, A&A, 343, L70

Surace, J., Sanders, D.B. 2000, ApJ, 120, 604

Tacconi, L., Genzel, R., Lutz, D., Rigopoulou, D., Baker, A.J., Iserlohe, C., Tecza, M. 2002, ApJ, 580, 73

Totani, T., Yoshii, Y., Iwamuro, F., Maihara, T., Motohara, K. 2001a, ApJ, 558, L57

Totani, T., Yoshii, Y., Maihara, T., Iwamuro, F., Motohara, K. 2001b, ApJ, 559, 592

Trentham, N., Kormendy, J., Sanders, D.B. 1999, AJ, 117, 2152

van Dokkum, P.G., et al. 2003, ApJ, 587, L83

Webb, T.M., et al. 2003a, ApJ, 587, 41

Webb, T. M. A., Lilly, S. J., Clements, D. L., Eales, S., Yun, M., Brodwin, M., Dunne, L., & Gear, W. K. 2003, ApJ, 597, 680

Wiklind, T. 2003, ApJ, 588, 736

Yun, M.S., Carilli, C.L. 2002, ApJ, 568, 88

Zheng, Z., Wu, H., Mao, S., Xia, X.-Y., Deng, Z.-G., Zou, Z.-L. 1999, A&A, 349, 735

Table 1. NDF MAMBO sources and associated 1.4GHz radio sources

	MAMBO 1.2mm properties				VLA 1.4GHz properties						
Source	No	RA (J2000)	DEC (J2000)	$S_{1.2mm}$ mJy	RA (J2000)	DEC (J2000)	$S_{1.4}$ μJy	Sep arcsec	P	Q	Comment
(1)	(2)	(3)	(4)	(5)	(6)	(7)	(8)	(9)	(10)	(11)	(12)
MMJ120507-0748.1	03	12:05:07.96	-07:48:11.9	4.6±1.0	12:05:08.12±0.03	-07:48:11.6±0.6	88	2.4	0.009	g	
MMJ120508-0743.1	26	12:05:08.36	-07:43:06.8	2.7±0.7	12:05:08.66±0.06	-07:43:05.6±1.2	42	4.6	0.107	u	
MMJ120509-0740.0	34	12:05:09.75	-07:40:02.5	3.3±0.6	12:05:09.80±0.05	-07:40:06.6±1.1	47	4.1	0.072	u	
MMJ120510-0747.0	10	12:05:10.97	-07:47:00.4	3.1±0.8	12:05:10.88±0.06	-07:46:57.6±1.3	41	3.1	0.074	u	
MMJ120516-0739.4	36	12:05:16.21	-07:39:27.1	2.2±0.6	12:05:16.06±0.03	-07:39:25.6±0.5	459	2.7	0.002	g	
MMJ120517-0743.1	25	12:05:17.93	-07:43:06.9	4.3±0.6	12:05:17.88±0.06	-07:43:09.6±1.3	40	2.8	0.070	u	
					12:05:17.86±0.02	-07:43:08.5±0.2					PdBI pos.
MMJ120519-0749.5	01	12:05:19.98	-07:49:33.8	5.2±1.0	12:05:19.90±0.04	-07:49:35.6±0.7	72	2.2	0.009	g	
MMJ120520-0738.9	39	12:05:20.45	-07:38:56.7	2.7±0.8	12:05:20.63±0.03	-07:38:55.6±0.5	336	2.9	0.003	g	
MMJ120522-0745.1	18	12:05:22.86	-07:45:10.0	2.0±0.5	12:05:23.12±0.03	-07:45:14.6±0.6	90	6.0	0.035	g	
MMJ120524-0747.3	08	12:05:24.86	-07:47:20.9	2.0±0.6	12:05:24.81±0.05	-07:47:23.6±1.1	47	2.8	0.042	u	
					12:05:24.54±0.05	-07:47:20.6±1.1	48	4.8	0.082	u	
MMJ120526-0746.6	13	12:05:26.85	-07:46:41.8	2.6±0.6	12:05:26.76±0.06	-07:46:40.6±1.3	41	1.8	0.035	g	
MMJ120530-0741.6	29	12:05:30.17	-07:41:41.2	2.3±0.6	12:05:30.25±0.03	-07:41:45.6±0.6	85	4.5	0.024	g	
MMJ120530-0747.7	07	12:05:30.85	-07:47:43.9	3.0±0.8	12:05:31.07±0.06	-07:47:39.6±1.3	40	5.4	0.134	u	
MMJ120531-0748.1	04	12:05:31.41	-07:48:07.2	2.7±0.9	12:05:31.13±0.05	-07:48:05.5±1.0	53	4.4	0.058	u	
MMJ120534-0738.3	42	12:05:34.81	-07:38:20.2	>2.2±0.9*	12:05:34.89±0.04	-07:38:18.5±0.9	61	2.1	0.012	g	
					12:05:34.49±0.06	-07:38:17.6±1.3	41	5.5	0.130	u	
MMJ120539-0745.4	16	12:05:39.37	-07:45:24.7	3.4±0.7	12:05:39.48±0.05	-07:45:26.5±1.0	55	2.4	0.020	u	
					12:05:39.47±0.02	-07:45:27.0±0.3					PdBI pos.
MMJ120545-0738.8	40	12:05:45.98	-07:38:51.8	3.7±0.8	12:05:45.72±0.06	-07:38:52.5±1.3	40	3.9	0.102	u	
MMJ120546-0741.5	31	12:05:46.56	-07:41:33.2	6.5±0.9	12:05:46.53±0.06	-07:41:32.5±1.2	42	0.8	0.009	g	
					12:05:46.59±0.02	-07:41:34.3±0.4					PdBI pos.

Note. — Col. (1) — MAMBO source.
Col. (2) — Short number on the original MAMBO NDF source list.
Col. (3)-(4) — J2000 coordinates of the source in the MAMBO data.
Col. (5) — MAMBO 1.2mm peak flux density. *: The source MMJ120534-0738.3 appears to be extended and may be multiple or smeared. For consistency with the other sources, we list its peak flux which is effectively a lower limit to the true flux. The source was included because of a reliable detection in total flux and a 1.4GHz counterpart.
Col. (6)-(7) — J2000 coordinates of the associated radio source.
Col. (8) — VLA 1.4GHz peak flux density. The average rms of the radio map is 13 μJy. See also col. (11) for possible effects of striping residuals caused by bright sources contained in the radio map (see § 2).
Col. (9) — Separation between MAMBO position and VLA position.
Col. (10) — Probability that the association is a chance coincidence.
Col. (11) — Quality flag for good (g) and uncertain (u) radio sources. To declare the quality of a radio source as good two criteria has to fulfilled: (1) source does not disappear in the 'background-subtracted' radio map, and (2) no eye-catching clustering of $>40\mu$Jy peaks in the adjacent region.

Table 2. Optical/near-infrared objects close to the interferometric positions

Source (1)	RA (J2000) (2)	DEC (J2000) (3)	Sep arcsec (4)	B mag (5)	V mag (6)	R mag (7)	I mag (8)	z mag (9)	J mag (10)	K mag (11)	z_{phot} (12)	P (13)
03a	12:05:08.07	-07:48:11.7	0.8	≈27.1	>26.5	!25.9	>25.5	≈26.1	!23.3	21.48	$2.11^{+0.26}_{-0.61}$	0.030
03b	12:05:07.97	-07:48:08.7	3.7	>27.4	>26.5	!25.8	≈25.3	25.48	>24.0	≈21.9	$3.64^{+0.84}_{-0.50}$	
03c	12:05:08.03	-07:48:17.5	6.1	24.93	24.49	24.11	23.42	23.94	22.00	20.36	$1.48^{+0.11}_{-0.09}$	
03d*	12:05:08.34	-07:48:16.7	6.1	>27.4	>26.5	≈25.3	≈25.0	>26.4	>24.0	>22.0	$3.86^{+0.56}_{-0.39}$	
03e	12:05:07.89	-07:48:05.9	6.7	24.75	23.90	22.82	22.09	22.61	20.78	19.27	$0.41^{+0.03}_{-0.01}$	
26a	12:05:08.48	-07:43:02.7	4.0	≈26.7	!26.3	!25.3	!24.8	≈25.6	>24.0	>22.0	$0.56^{+0.13}_{-0.17}$	
26b	12:05:08.29	-07:43:05.9	5.5	!26.9	!25.6	!25.8	≈24.8	≈26.2	>24.0	>22.0	$2.91^{+0.31}_{-0.23}$	
26c	12:05:08.30	-07:43:07.5	5.7	!27.1	>26.5	25.04	23.88	24.80	23.30	>22.0	$0.67^{+0.07}_{-0.11}$	
26d	12:05:08.99	-07:43:00.2	7.3	25.22	24.97	24.22	≈24.6	24.50	≈22.6	20.96	$2.29^{+0.04}_{-0.07}$	
26e	12:05:08.51	-07:42:58.6	7.4	25.62	≈25.5	!25.4	>25.5	≈25.7	>24.0	>22.0	$1.28^{+1.55}_{-0.71}$	
34a	12:05:09.51	-07:40:04.5	4.8	22.88	22.69	21.83	21.45	22.28	20.73	19.56	$0.51^{+0.02}_{-0.01}$	
34b	12:05:09.69	-07:40:01.5	5.3	23.48	22.92	21.88	21.25	21.77	20.13	18.65	$0.46^{+0.02}_{-0.01}$	
34c	12:05:10.16	-07:40:04.0	5.9	22.76	21.60	20.59	19.82	20.42	18.59	17.14	$0.40^{+0.01}_{-0.01}$	
34d	12:05:09.29	-07:40:07.0	7.6	24.92	24.59	23.56	23.02	23.63	22.19	21.03	$0.53^{+0.03}_{-0.04}$	
34e	12:05:10.33	-07:40:08.5	8.1	25.50	≈25.5	24.60	23.77	24.24	≈22.6	21.08	$1.27^{+0.06}_{-0.07}$	
10a1	12:05:10.95	-07:47:00.0	2.6	24.43	24.26	23.40	23.08	23.48	22.04	20.24	$0.54^{+0.03}_{-0.04}$	0.130
10a2	12:05:10.85	-07:47:00.0	2.4	!25.9°	≈25.55°	≈25.0°	!24.8°	!25.6°	>24.0	20.58	$2.49^{+0.01}_{-0.05}$	0.136
10b	12:05:10.94	-07:46:54.0	3.6	24.41	23.92	23.29	22.56	23.04	20.65	19.17	$2.09^{+0.06}_{-0.05}$	
10c	12:05:11.06	-07:46:54.5	4.1	22.96	22.42	21.72	21.37	22.08	20.65	20.17	$0.41^{+0.01}_{-0.01}$	
10d	12:05:10.65	-07:46:54.8	4.3	25.44	25.13	24.15	23.21	23.96	22.16	20.94	$0.60^{+0.09}_{-0.07}$	
10e	12:05:10.51	-07:47:00.0	6.0	25.66	≈25.9	25.08	≈24.6	≈25.8	!23.5	!21.9	$0.55^{+0.16}_{-0.11}$	
36a	12:05:16.05	-07:39:25.2	0.4	!27.1	>26.5	>26.2	≈24.9	25.71	22.33	20.11	$1.70^{+0.12}_{-0.20}$	0.006
36b	12:05:15.87	-07:39:27.3	3.4	25.31	25.14	24.98	24.17	25.06	22.85	≈21.4	$1.55^{+0.24}_{-0.12}$	
36c	12:05:16.07	-07:39:21.0	4.6	26.40	>26.5	>26.2	>25.5	>26.4	>24.0	>22.0	$0.78^{+1.90}_{-0.78}$	
36d	12:05:15.62	-07:39:24.8	6.6	>27.4	>26.5	≈25.3	>25.5	≈25.9	>24.0	>22.0	$4.04^{+0.38}_{-0.63}$	
36e	12:05:16.54	-07:39:26.5	7.2	24.65	24.63	23.72	23.11	23.40	21.41	20.19	$1.40^{+0.01}_{-0.02}$	
25a	12:05:17.89	-07:43:08.6	0.4	≈26.1	≈25.3	≈25.4	>25.5	25.87	>24.0	22.5$^{\bullet}$	$2.91^{+0.12}_{-0.14}$	0.020
25b	12:05:18.24	-07:43:08.5	5.7	25.26	25.14	24.73	24.21	24.61	22.79	>22.0	$1.41^{+0.07}_{-0.11}$	
25c	12:05:17.36	-07:43:11.2	7.8	26.22	25.90	25.02	25.11	25.90	>24.0	>22.0	$3.60^{+0.08}_{-0.17}$	
25d	12:05:18.40	-07:43:09.3	8.1	25.04	24.52	23.42	22.41	22.80	21.02	19.38	$0.61^{+0.03}_{-0.03}$	
25e	12:05:18.24	-07:43:14.7	8.4	25.55	25.44	24.70	23.97	24.61	22.30	20.73	$2.01^{+0.25}_{-0.59}$	
01b	12:05:20.08	-07:49:33.6	3.4	25.59†	≈25.5†	24.49†	24.63†	24.96†	23.28	20.31	$0.50^{+0.04}_{-0.05}$	
01c	12:05:19.74	-07:49:32.0	4.2	24.84	23.93	23.25	22.88	23.46	21.93	20.35	$0.35^{+0.01}_{-0.01}$	
39a	12:05:20.59	-07:38:55.4	0.6	25.43	25.14	24.17	22.73	23.19	20.99	19.04	$1.32^{+0.04}_{-0.01}$	0.005
39d	12:05:20.22	-07:38:55.0	6.2	26.24	>26.5	25.17	>25.5	25.70	≈23.3	>22.0	$2.23^{+0.16}_{-0.25}$	
39e	12:05:20.66	-07:39:02.6	7.1	22.75	22.07	21.26	20.74	21.50	19.77	19.20	$0.36^{+0.05}_{-0.02}$	
39f	12:05:20.24	-07:38:49.9	8.1	24.76	24.54	23.49	22.12	22.43	20.14	18.35	$1.37^{+0.02}_{-0.01}$	
18a	12:05:23.13	-07:45:14.9	0.3	≈26.9	>26.5	24.87	23.34	23.59	21.56	19.61	$1.25^{+0.06}_{-0.06}$	0.003
18b	12:05:23.30	-07:45:15.8	2.9	!27.1	≈26.2	≈25.8	!25.3	≈25.6	>24.0	>22.0	$3.10^{+0.40}_{-0.54}$	
18c	12:05:22.93	-07:45:13.0	3.2	25.75	≈26.3	≈26.1	24.37	25.38	≈23.4	21.40	$1.29^{+0.10}_{-0.25}$	
18d	12:05:22.88	-07:45:16.8	4.3	25.29	24.55	23.55	22.60	22.85	20.64	18.69	$2.40^{+0.03}_{-0.02}$	
18e	12:05:23.36	-07:45:11.5	4.6	≈26.9	>26.5	≈25.1	>25.5	≈26.2	>24.0	>22.0	$3.77^{+0.12}_{-0.23}$	
08a	12:05:24.65	-07:47:20.5	3.8	≈27.2	>26.5	≈25.8	≈25.0	≈25.6	>24.0	>22.0	$0.66^{+0.20}_{-0.29}$	
08b	12:05:25.06	-07:47:19.5	5.6	>27.4	>26.5	>26.2	≈24.8	25.58	!23.8	>22.0	$5.25^{+0.40}_{-0.76}$	
08c	12:05:24.94	-07:47:17.6	6.3	25.18	24.66	23.91	22.89	23.45	21.81	20.48	$0.74^{+0.04}_{-0.06}$	
08d	12:05:24.30	-07:47:22.5	7.6	26.59	>26.5	>26.2	>25.5	!26.0	>24.0	>22.0	$1.23^{+0.29}_{-0.70}$	
08e	12:05:24.75	-07:47:15.9	7.7	26.09	≈26.1	>26.2	>25.5	>26.4	>24.0	>22.0	$0.91^{+1.75}_{-0.91}$	
13a	12:05:26.78	-07:46:41.0	0.5	≈26.5	>26.5	!25.6	!24.9	!25.7	≈23.1	20.44	$2.26^{+0.21}_{-0.59}$	0.014
13c	12:05:26.96	-07:46:45.3	5.6	≈26.8	>26.5	25.30	24.84	25.63	!23.4	>22.0	$0.50^{+0.12}_{-0.50}$	
13d	12:05:26.78	-07:46:34.9	5.7	24.87	24.52	23.91	23.51	23.80	22.33	21.40	$1.36^{+0.08}_{-0.04}$	
13e	12:05:26.29	-07:46:39.4	7.1	25.17	24.90	23.66	23.11	23.77	22.21	20.99	$0.53^{+0.03}_{-0.02}$	
29a	12:05:30.26	-07:41:45.4	0.2	25.48	25.17	24.46	24.01	25.06	22.60	20.68	$2.26^{+0.10}_{-0.10}$	0.003
29b	12:05:30.17	-07:41:46.8	1.8	25.33	24.84	24.44	24.44	25.25	22.88	21.40	$2.34^{+0.07}_{-0.09}$	

Table 2—Continued

Source	RA (J2000)	DEC (J2000)	Sep arcsec	B mag	V mag	R mag	I mag	z mag	J mag	K mag	z_{phot}	P
(1)	(2)	(3)	(4)	(5)	(6)	(7)	(8)	(9)	(10)	(11)	(12)	(13)

Table 2—Continued

Source	RA (J2000)	DEC (J2000)	Sep arcsec	B mag	V mag	R mag	I mag	z mag	J mag	K mag	z_{phot}	P
(1)	(2)	(3)	(4)	(5)	(6)	(7)	(8)	(9)	(10)	(11)	(12)	(13)

Table 2—Continued

Source	RA	DEC	Sep	B	V	R	I	z	J	K	z_{phot}	P
	(J2000)	(J2000)	arcsec	mag	mag	mag	mag	mag	mag	mag		
(1)	(2)	(3)	(4)	(5)	(6)	(7)	(8)	(9)	(10)	(11)	(12)	(13)

Table 2—Continued

Source (1)	RA (J2000) (2)	DEC (J2000) (3)	Sep arcsec (4)	B mag (5)	V mag (6)	R mag (7)	I mag (8)	z mag (9)	J mag (10)	K mag (11)	z_{phot} (12)	P (13)

Table 2—Continued

Source	RA (J2000)	DEC (J2000)	Sep arcsec	B mag	V mag	R mag	I mag	z mag	J mag	K mag	z_{phot}	P
(1)	(2)	(3)	(4)	(5)	(6)	(7)	(8)	(9)	(10)	(11)	(12)	(13)

Table 2—Continued

Source	RA	DEC	Sep	B	V	R	I	z	J	K	z_{phot}	P
	(J2000)	(J2000)	arcsec	mag	mag	mag	mag	mag	mag	mag		
(1)	(2)	(3)	(4)	(5)	(6)	(7)	(8)	(9)	(10)	(11)	(12)	(13)

Table 2—Continued

Source	RA (J2000)	DEC (J2000)	Sep arcsec	B mag	V mag	R mag	I mag	z mag	J mag	K mag	z_{phot}	P
(1)	(2)	(3)	(4)	(5)	(6)	(7)	(8)	(9)	(10)	(11)	(12)	(13)

Table 2—Continued

Source	RA (J2000)	DEC (J2000)	Sep arcsec	B mag	V mag	R mag	I mag	z mag	J mag	K mag	z_{phot}	P
(1)	(2)	(3)	(4)	(5)	(6)	(7)	(8)	(9)	(10)	(11)	(12)	(13)

Table 2—Continued

Source	RA (J2000)	DEC (J2000)	Sep arcsec	B mag	V mag	R mag	I mag	z mag	J mag	K mag	z_{phot}	P
(1)	(2)	(3)	(4)	(5)	(6)	(7)	(8)	(9)	(10)	(11)	(12)	(13)

Table 2—Continued

Source	RA (J2000)	DEC (J2000)	Sep arcsec	B mag	V mag	R mag	I mag	z mag	J mag	K mag	z_{phot}	P
(1)	(2)	(3)	(4)	(5)	(6)	(7)	(8)	(9)	(10)	(11)	(12)	(13)

Table 2—Continued

Source (1)	RA (J2000) (2)	DEC (J2000) (3)	Sep arcsec (4)	B mag (5)	V mag (6)	R mag (7)	I mag (8)	z mag (9)	J mag (10)	K mag (11)	z_{phot} (12)	P (13)
29c	12:05:30.13	-07:41:44.2	2.3	!27.3	>26.5	!25.6	>25.5	>26.4	>24.0	21.23	$2.70^{+0.48}_{-0.34}$	
29d	12:05:29.91	-07:41:46.4	5.2	26.11	≈26.0	>26.2	>25.5	26.01	>24.0	>22.0	$1.23^{+1.69}_{-1.23}$	
29e	12:05:30.00	-07:41:51.2	6.9	26.59	≈26.1	≈25.8	24.80	25.68	≈23.1	>22.0	$1.72^{+0.34}_{-0.21}$	
07a	12:05:31.01	-07:47:39.9	0.9	26.06	≈25.6	≈25.2	>25.5	25.34	>24.0	>22.0	$0.35^{+0.34}_{-0.35}$	0.108
07b	12:05:31.19	-07:47:37.1	3.1	>27.4	>26.5	25.33	!25.2	25.61	≈23.3	≈21.9	$2.49^{+0.17}_{-0.18}$	
07c	12:05:30.87	-07:47:44.2	5.5	≈26.4	!26.0	24.66	23.64	24.25	22.14	21.53	$0.47^{+0.09}_{-0.47}$	
07d	12:05:31.30	-07:47:34.7	6.0	26.23	25.29	24.81	!24.9	26.05	>24.0	>22.0	$3.67^{+0.06}_{-0.09}$	
07e	12:05:30.64	-07:47:39.9	6.3	23.39	22.81	22.12	21.74	22.48	21.04	20.51	$0.41^{+0.01}_{-0.01}$	
04a	12:05:31.17	-07:48:04.7	1.0	22.39*	21.64*	21.14*	20.27*	20.89	19.02	17.36	$0.25^{+0.03}_{-0.04}$	0.005
04b	12:05:31.01	-07:48:07.1	2.3	23.43*	23.32*	23.23*	22.31	23.09	21.14	19.51	$1.39^{+0.06}_{-0.01}$	
04d	12:05:31.21	-07:48:11.0	5.5	25.97	!26.1	>26.2	≈25.3	25.41	22.30	20.33	$1.83^{+0.01}_{-0.05}$	
04e	12:05:31.47	-07:48:08.6	5.9	23.52	22.80	21.81	21.10	21.68	20.08	18.57	$0.41^{+0.05}_{-0.02}$	
42a	12:05:34.93	-07:38:17.4	1.3	>27.4	>26.5	>26.2	≈24.9	!25.7	!22.9	20.94	$1.52^{+0.24}_{-0.34}$	0.060
42b	12:05:34.96	-07:38:19.7	1.5	26.28	≈25.7	!25.4	!25.3	>26.4	>24.0	!21.5	$2.83^{+0.67}_{-0.24}$	0.082
42c	12:05:34.77	-07:38:17.7	2.0	>27.4	26.24	>26.2	>25.5	!25.5	>24.0	21.33	$3.10^{+0.34}_{-0.44}$	
42d	12:05:35.06	-07:38:22.0	4.2	>27.4	>26.5	>26.2	!25.4	>26.4	>24.0	21.04	$4.21^{+0.79}_{-1.67}$	
16a	12:05:39.61	-07:45:27.9	2.3	25.54	25.30	24.85	23.63	24.32	≈23.8	21.11	$0.93^{+0.13}_{-0.08}$	
16b	12:05:39.35	-07:45:28.7	2.4	25.47	25.27	24.78	23.88	24.95	22.21	20.50	$1.70^{+0.19}_{-0.12}$	
16c	12:05:39.54	-07:45:24.3	2.9	25.20	24.58	23.59	23.06	23.59	21.97	20.45	$0.46^{+0.02}_{-0.02}$	
16d	12:05:39.19	-07:45:22.7	6.0	26.21	≈26.3	≈26.0	24.62	25.16	≈23.5	≈21.9	$1.13^{+0.26}_{-0.17}$	
16e	12:05:39.93	-07:45:25.0	7.1	26.05	!26.4	≈25.4	≈25.0	25.65	>24.0	>22.0	$0.58^{+0.18}_{-0.10}$	
40a	12:05:45.69	-07:38:50.5	2.1	26.33	≈26.1	≈25.9	!25.0	!26.1	!23.7	!21.7	$1.61^{+0.92}_{-0.25}$	0.168
40b	12:05:45.98	-07:38:51.8	3.9	>27.4	>26.5	>26.2	!25.3	≈25.8	22.19	19.57	$1.52^{+1.24}_{-0.25}$	
40c	12:05:45.55	-07:38:48.4	4.8	≈26.7	>26.5	≈25.2	!25.2	25.40	>24.0	>22.0	$0.54^{+0.09}_{-0.10}$	
40d	12:05:45.69	-07:38:59.1	6.6	25.24	24.63	23.92	23.60	23.99	!23.2	21.41	$3.41^{+0.05}_{-0.08}$	
31a	12:05:46.69	-07:41:30.3	4.3	25.80	25.04	≈24.8	≈23.8	25.12	!23.6	≈21.8	$2.87^{+0.11}_{-0.17}$	
31b	12:05:46.94	-07:41:33.3	5.3	25.52	25.70	25.33	≈24.7	25.08	≈23.1	>22.0	$1.35^{+0.15}_{-0.08}$	
31c	12:05:46.65	-07:41:39.5	5.3	25.72	25.23	24.48	23.30	23.75	22.29	20.37	$1.11^{+0.05}_{-0.03}$	
31d	12:05:46.82	-07:41:38.9	5.7	≈26.8	>26.5	25.01	23.82	24.58	≈23.0	>22.0	$0.70^{+0.09}_{-0.08}$	

Note. — Col. (1) — Optical/near-infrared source identification. Suggested counterparts to mm sources are marked in bold.
Col. (2)-(3) — J2000 coordinates of optical/near-infrared source.
Col. (4) — Separation between optical position and best interferometric position.
Col. (5)-(11) — Source magnitudes in a 2″ aperture. All magnitudes are on the Vega system except for the z magnitudes which are on the BD system (see text).
Col. (12) — Optical/near-infrared photometric redshift.
Col. (13) — Probability of a chance coincidence with an object of the given K magnitude (07a: B) at the given separation.
†: magnitude contaminated by nearby foreground galaxy.
∗: magnitude contaminated by nearby foreground star.
⋆: 03d is not detected in B,z and K but retained due to credible R and I detections.
∘: magnitude contaminated by 10a1.
•: Lehnert et al. (2004, in preparation).

Table 3. Main properties of counterparts to MAMBO sources

Source	No	Q	$S_{1.2mm}$ mJy	$S_{1.4}$ μJy	K mag	z_{CY}	z_{phot}	$z_{submm/mm}$
(1)	(2)	(3)	(4)	(5)	(6)	(7)	(8)	(9)
MMJ120507-0748.1	03	g	4.6	88	21.48	$2.38^{+1.19}_{-0.76}$	$2.11^{+0.26}_{-0.61}$	$4.25^{+\infty}_{-4.25}$
MMJ120508-0743.1	26	u	2.7	42	>22.0	$2.64^{+1.55}_{-0.95}$		
MMJ120509-0740.0	34	u	3.3	47	>22.0	$2.73^{+1.49}_{-0.91}$		(see note)
MMJ120510-0747.0	10	u	3.1	41	20.58	$2.82^{+1.74}_{-1.00}$	$2.49^{+0.01}_{-0.05}$	
MMJ120516-0739.4	36	g	2.2	459	20.11	$0.83^{+0.42}_{-0.34}$	$1.70^{+0.12}_{-0.20}$	
MMJ120517-0743.1	25	g	4.3	40	22.50	$3.27^{+2.07}_{-1.08}$	$2.91^{+0.12}_{-0.14}$	$3.65^{+4.26}_{-2.53}$
MMJ120519-0749.5	01	g	5.2	72	>22.0	$2.74^{+1.41}_{-0.87}$		> 8.95
MMJ120520-0738.9	39	g	2.7	336	19.04	$1.05^{+0.50}_{-0.39}$	$1.32^{+0.04}_{-0.01}$	
MMJ120522-0745.1	18	g	2.0	90	19.61	$1.67^{+0.79}_{-0.58}$	$1.25^{+0.06}_{-0.06}$	
MMJ120524-0747.3	08	u	2.0	47	>22.0	$2.21^{+1.25}_{-0.79}$		
MMJ120526-0746.6	13	g	2.6	41	20.44	$2.62^{+1.54}_{-0.92}$	$2.26^{+0.21}_{-0.59}$	
MMJ120530-0741.6	29	g	2.3	85	20.68	$1.82^{+0.88}_{-0.63}$	$2.26^{+0.10}_{-0.10}$	
MMJ120530-0747.7	07	u	3.0	40	>22.0	$2.82^{+1.77}_{-1.00}$	$(0.35^{+0.34}_{-0.35})$	
MMJ120531-0748.1	04	u	2.7	53	>18.0	$2.37^{+1.32}_{-0.86}$	$(0.25^{+0.03}_{-0.04})$	
MMJ120534-0738.3	42	g	2.2	61	20.94	$2.05^{+1.14}_{-0.79}$	$1.52^{+0.24}_{-0.34}$	
MMJ120539-0745.4	16	g	3.4	55	>22.7	$2.56^{+1.37}_{-0.84}$		$6.35^{+\infty}_{-4.85}$
MMJ120545-0738.8	40	u	3.7	40	19.57	$3.05^{+1.97}_{-1.04}$	$1.52^{+1.24}_{-0.25}$	
MMJ120546-0741.5	31	g	6.5	42	21.90	$3.86^{+2.58}_{-1.31}$		$5.25^{+6.14}_{-1.93}$

Note. — Col. (1) — MAMBO source.
Col. (2) — Short number on the original MAMBO NDF source list.
Col. (3) — Quality of the interferometric identification. g(ood) stands for objects with a good quality VLA source or a PdBI identification.
Col. (4) — MAMBO 1.2mm peak flux density.
Col. (5) — VLA 1.4GHz peak flux density.
Col. (6) — K magnitude (Vega), see Table 2 for other bands. For MMJ120519-0749.5 and MMJ120531-0748.1, we give K-band limits as we assume that the foreground objects detected at the radio position are not linked to the dust emission.
Col. (7) — Redshift estimate from radio/mm spectral index (Carilli & Yun 2000b). Errors reflect 1σ uncertainties in alpha due to measurement errors and due to the intrinsic scatter of the relation, added in quadrature.
Col. (8) — Photometric redshift from optical/near-infrared photometry. Values in brackets refer to objects - MMJ120519-0749.5 and MMJ120531-0748.1 - that are likely in the foreground.
Col. (9) — Redshift estimate from the 1200μm/850μm flux ratio as derived by Eales et al. (2003). No. 34 was observed but the flux ratio could not be fit by the templates used at any redshift.

Fig. 1.— Histogram of separations between mm positions from the MAMBO map and VLA positions of associated radio sources. Light and dark grey indicate the good and uncertain sources from Table 1. The dashed histogram indicates the expected number of unrelated background radio peaks.

Fig. 2.— BRzK images (from left to right) for the fields of the MAMBO sources with radio associations. The $25'' \times 25''$ images are centered on the nominal MAMBO positions listed in Table 1 and oriented such that north is at the top and east to the left. A small cross indicates the best interferometric position (PdBI if available, VLA otherwise) and its 1σ error. The right panel indicates all $\geq 40\mu$Jy radio peaks by crosses, and the $7''$ radius used to search for radio peaks possibly associated with the MAMBO sources. Small letters label optical/near-infrared sources near to the best interferometric position (see also Table 2).

Fig. 3.— BzK color composites of the NDF MAMBO sources with interferometric positions. Large $7''$ radius circles are drawn around the nominal MAMBO positions. Unlike in Fig. 2, we now show both the VLA 1.4GHz peaks (indicated by squares) and position of the PdBI mm interferometric sources (indicated by small circles).

Fig. 4.— Comparison of optical/near-infrared photometric redshifts with redshift estimates from the radio/mm spectral index. Blank fields without photometric redshifts are shown with an arbitrary lower limit of 0.5 for the optical/near-infrared photometric redshift, and without the error bars for the radio/mm estimate. For two objects shown by squares we believe that the measured optical/NIR photometric redshift refers to a foreground object, the true redshift of the submm source being higher (see text).

Fig. 5.— Distribution of K and I magnitudes for the interferometrically located NDF 1.2mm objects and for three samples of interferometrically located SCUBA 850μm galaxies. The limit symbol at K>22, I> 25.5 in the NDF panel stands for 5 objects. In the panel for the 8mJy survey, we indicate the regions occupied in this type of diagram by the class 0/I/II objects in the definition used by Ivison et al. (2002). In the top two panels thick symbols reflect identifications described as good/robust. Magnitudes for the cluster lens sources have been corrected for the magnifications stated in the original papers.

Fig. 6.— I-K vs. K magnitude-color diagram for the MAMBO identifications (large filled circles). Small dots show the field galaxy population from our NDF data. Interferometrically located SCUBA galaxies are represented by squares for the 8mJy sample objects from Ivison et al. (2002), stars for cluster lens survey objects (corrected for magnification) from Smail et al. (2002), and triangles for the CUDSS objects of Webb et al. (2003a,b). Filled diamonds connected by continuous lines show the expected colors/magnitudes for redshift

1,2,. . . for objects with the SED shapes of Arp220 and IRAS 22491-1808 *but scaled to observed* $S_{1.2mm}$*=5mJy*. Average properties in magnitude bins are shown with error bars for the (sub)mm population (open diamonds) including all objects shown, and for the field population (crosses). Blank field sources are not included, the figure is an incomplete representation in its right part.

Fig. 7.— J-K color as a function of redshift for the template SED shapes of a number of local ultra-luminous infrared galaxies. Horizontal over-plotted lines show measurements (continuous) or lower limits (dashed) for the J-K color our MAMBO sources.

Fig. 8.— I-K vs. J-K diagram, with the thick dashed lines showing the regions populated by z$\sim$1-2 passive ellipticals and by dusty starbursts according to Pozzetti & Mannucci (2000). Triangles indicate NDF MAMBO sources. Diamonds indicate SCUBA sources from the literature with IJK photometry and one A2125 MAMBO source from Bertoldi et al. (2000). The thin vertical dashed line indicates the J-K$>$2.3 criterion of Franx et al. (2003).

Fig. 9.— Top panel: Diagnostic diagram for the near-infrared to radio SEDs of (sub)mm sources, combining the radio/submm spectral index with a spectral index between near-infrared and submm. Thick squares/limits represent the NDF MAMBO source discussed in this paper, thin asterisks/limits mostly SCUBA sources from the samples described in the text, and a few individual well studied (sub)mm objects. Objects with CO-confirmed redshifts are labeled with their redshift. A typical observational error is indicated in the lower left. The lower panel shows for comparison the loci corresponding to the redshifted SEDs of a number of local ULIRGs with available UV to radio SEDs. Note that IRAS 19254-7245 hosts a powerful AGN.

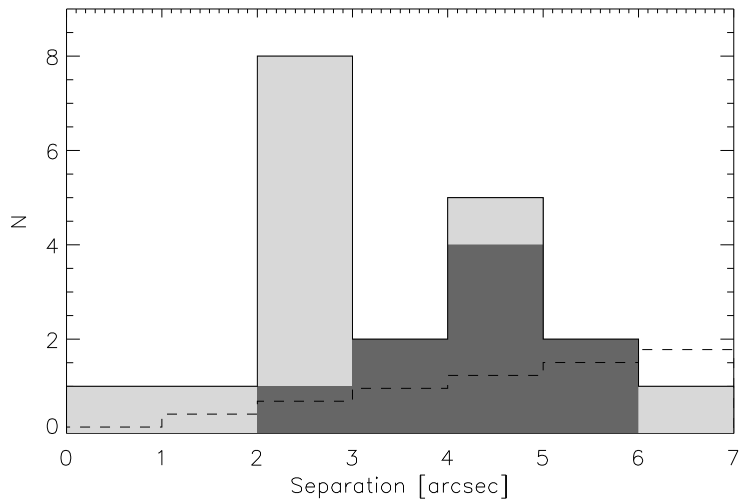
N
0
2
4
6
8
0
1
2
3
4
5
6
7
Separation [arcsec]

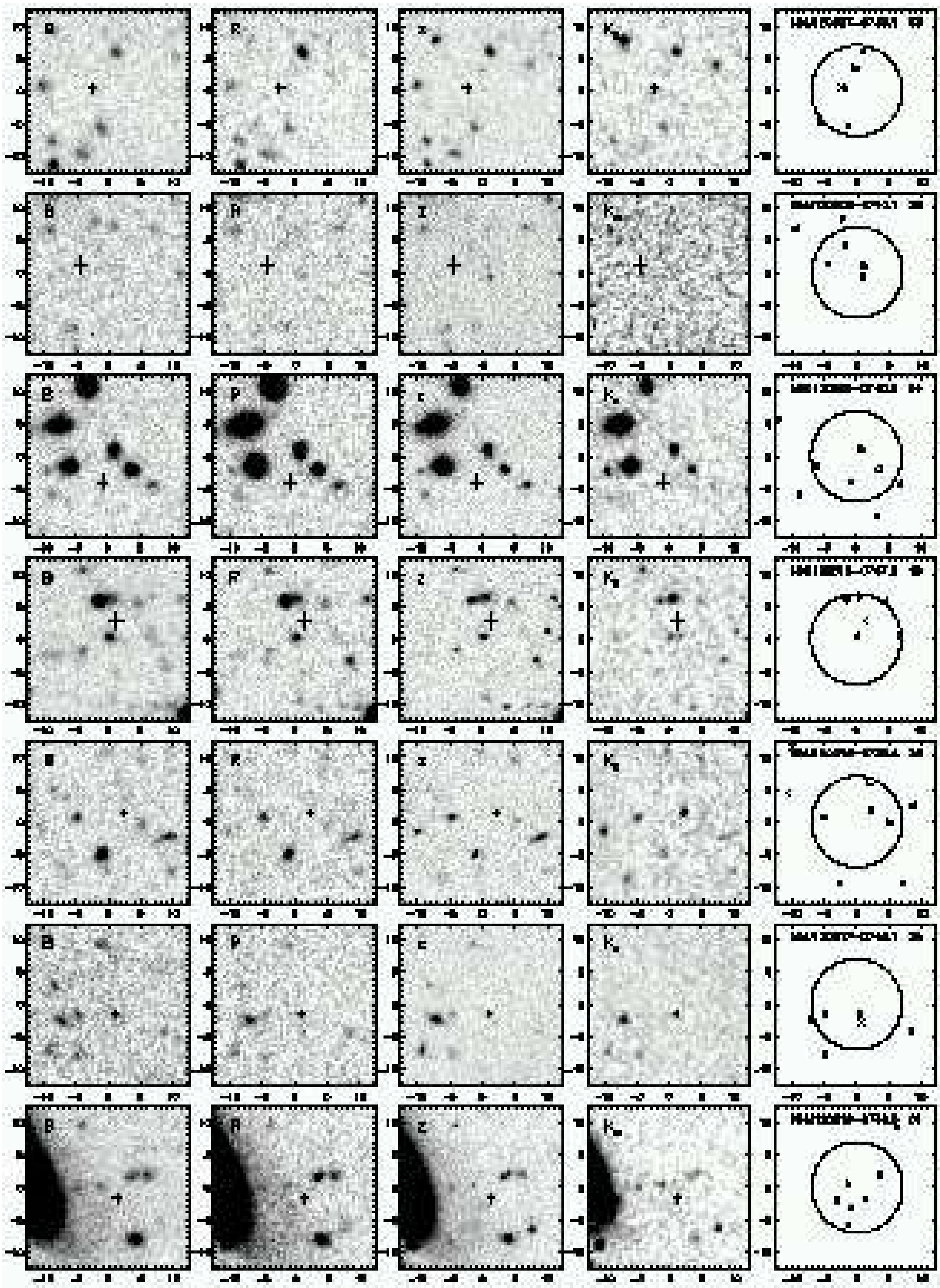

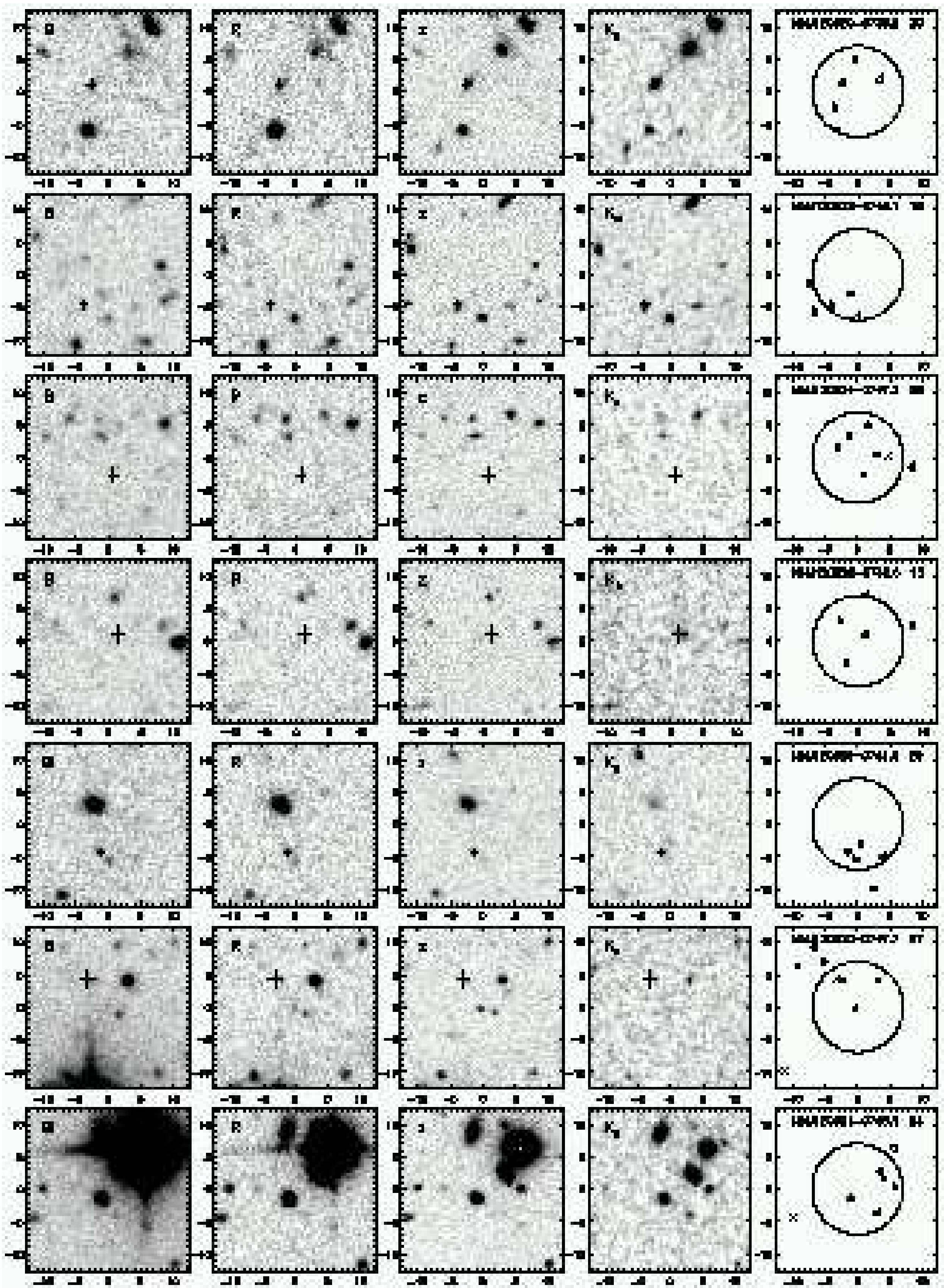

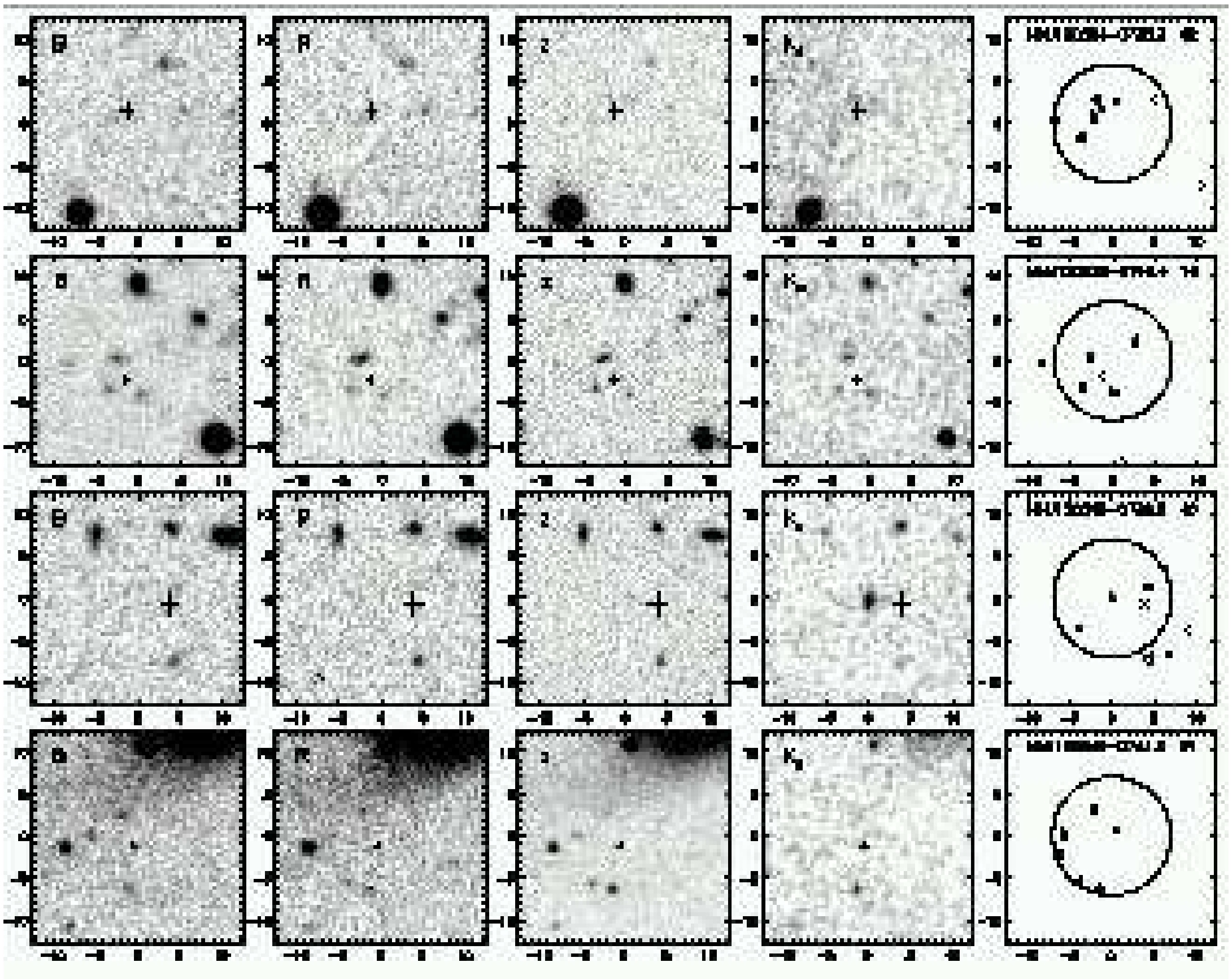

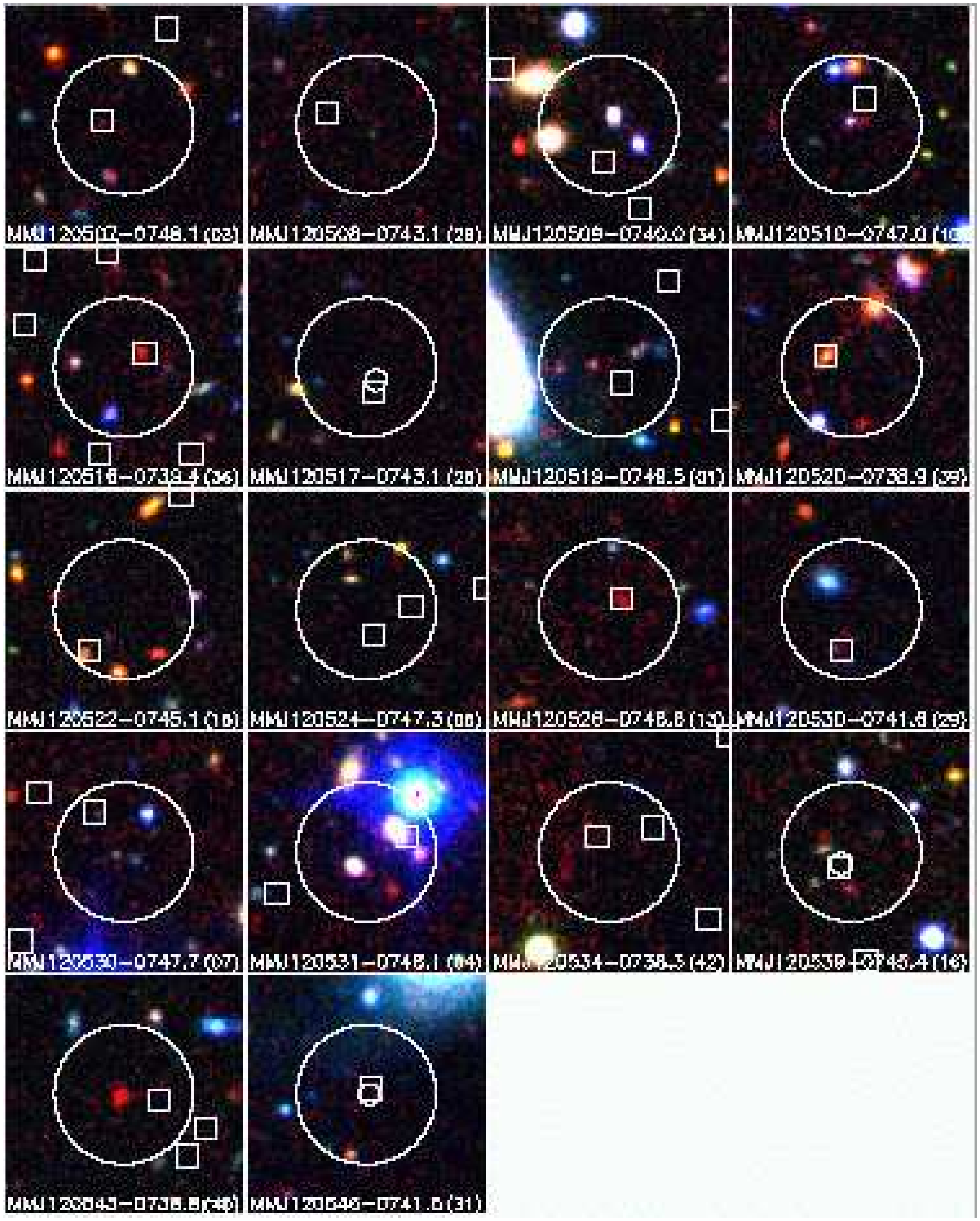
MMJ120507-0748.1 (02)
MMJ120508-0743.1 (28)
MMJ120509-0740.0 (34)
MMJ120510-0747.0
MMJ120516-0739.4 (36)
MMJ120517-0743.1 (26)
MMJ120519-0748.5 (01)
MMJ120520-0738.9 (39)
MMJ120522-0745.1 (18)
MMJ120524-0747.3 (08)
MMJ120528-0748.8 (13)
MMJ120530-0741.8 (29)
MMJ120530-0747.7 (07)
MMJ120531-0748.1 (04)
MMJ120534-0738.3 (42)
MMJ120539-0745.4 (16)
MMJ120546-0741.6 (31)

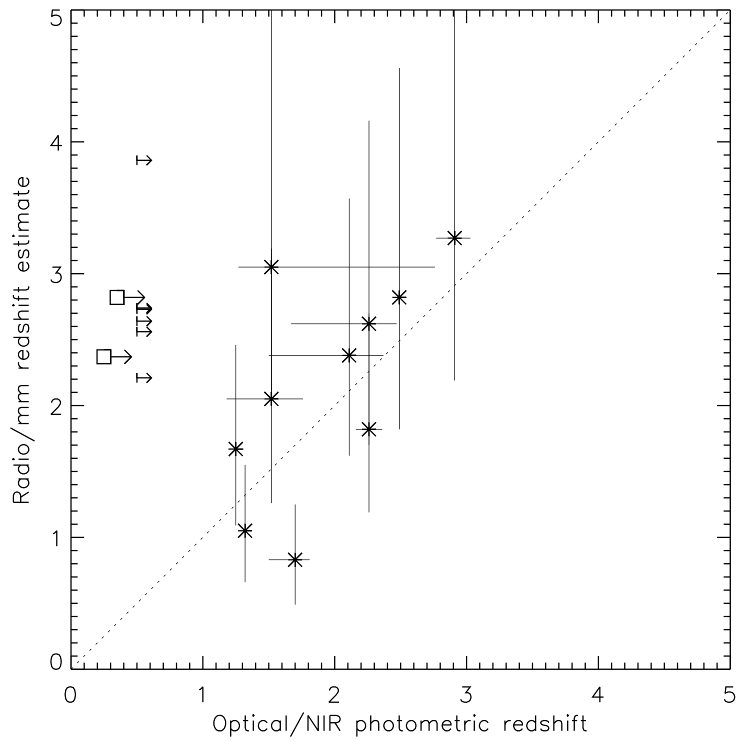
Radio/mm redshift estimate
Optical/NIR photometric redshift
0
1
2
3
4
5

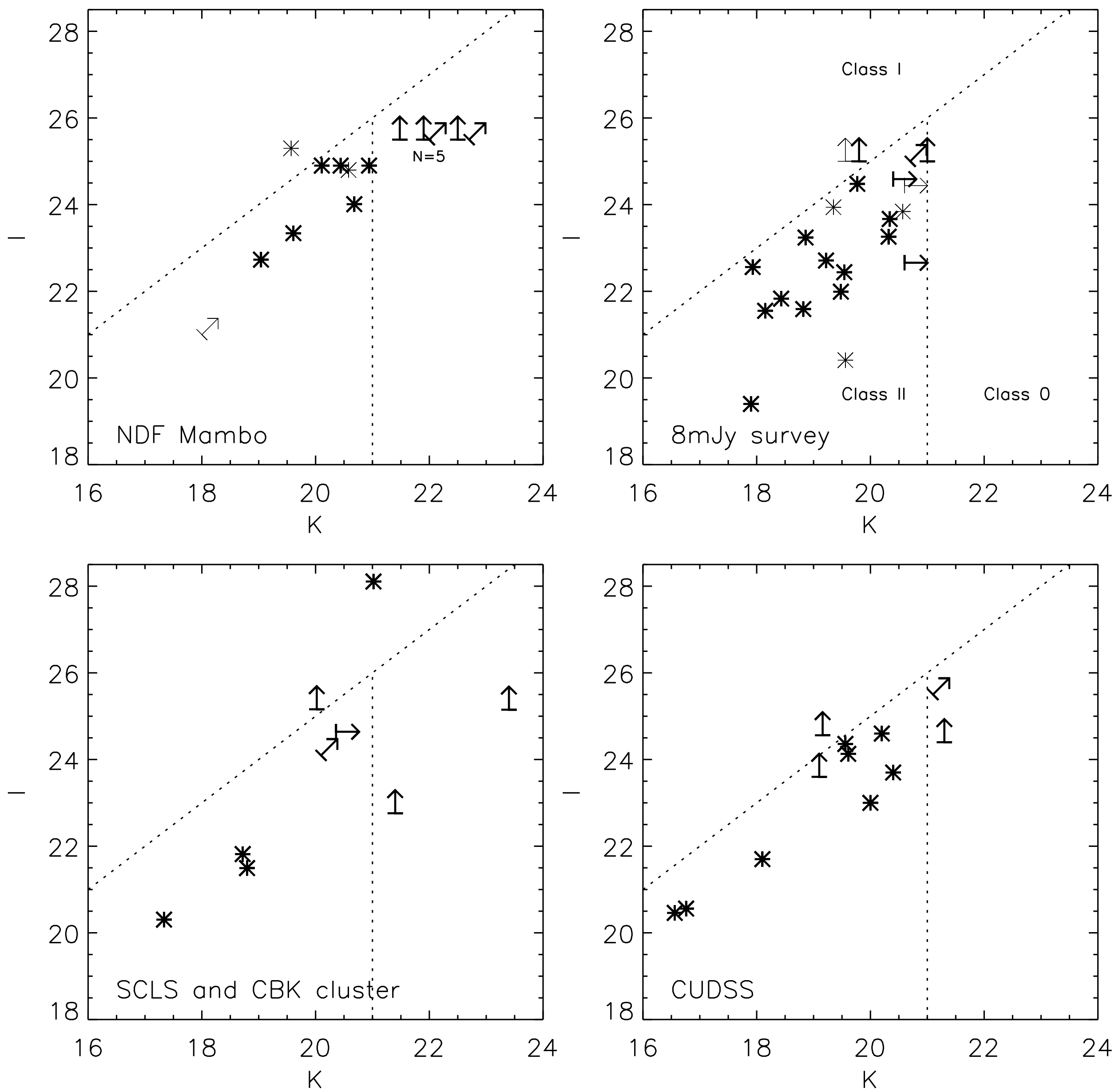
NDF Mambo
N=5
8mJy survey
Class I
Class II
Class 0
SCLS and CBK cluster
CUDSS
K
I

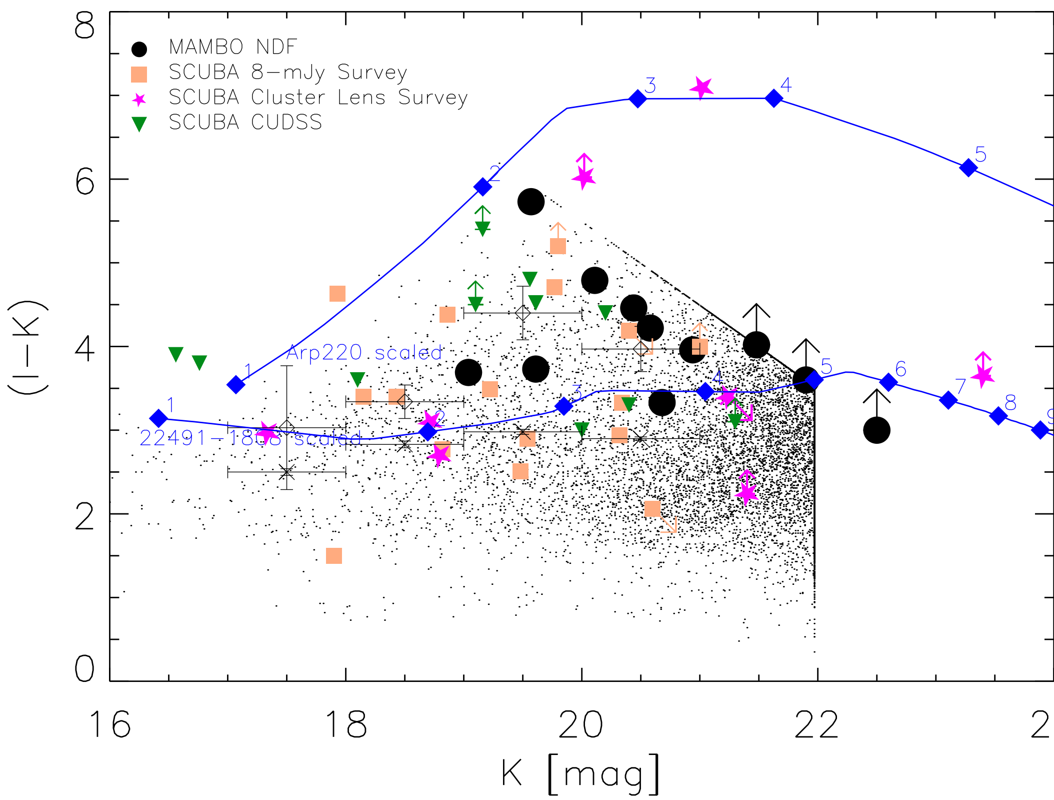
MAMBO NDF
SCUBA 8−mJy Survey
SCUBA Cluster Lens Survey
SCUBA CUDSS
Arp220 scaled
22491−1808 scaled
(I−K)
K [mag]
0
2
4
6
8
16
18
20
22
24

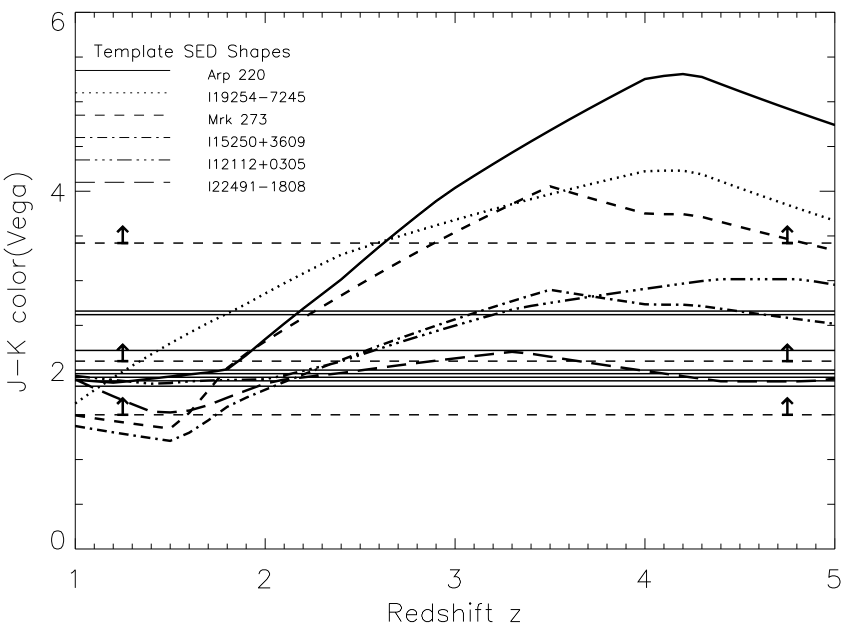
Template SED Shapes
Arp 220
I19254−7245
Mrk 273
I15250+3609
I12112+0305
I22491−1808
J−K color(Vega)
Redshift z
0
2
4
6
1
2
3
4
5

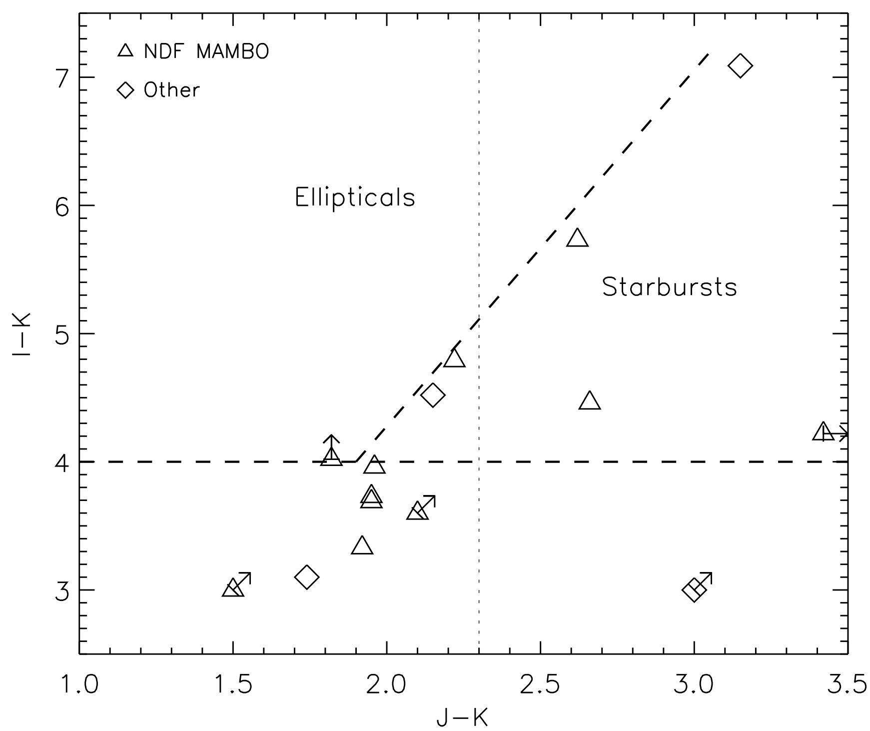
NDF MAMBO
Other
Ellipticals
Starbursts
I−K
J−K
7
6
5
4
3
1.0
1.5
2.0
2.5
3.0
3.5

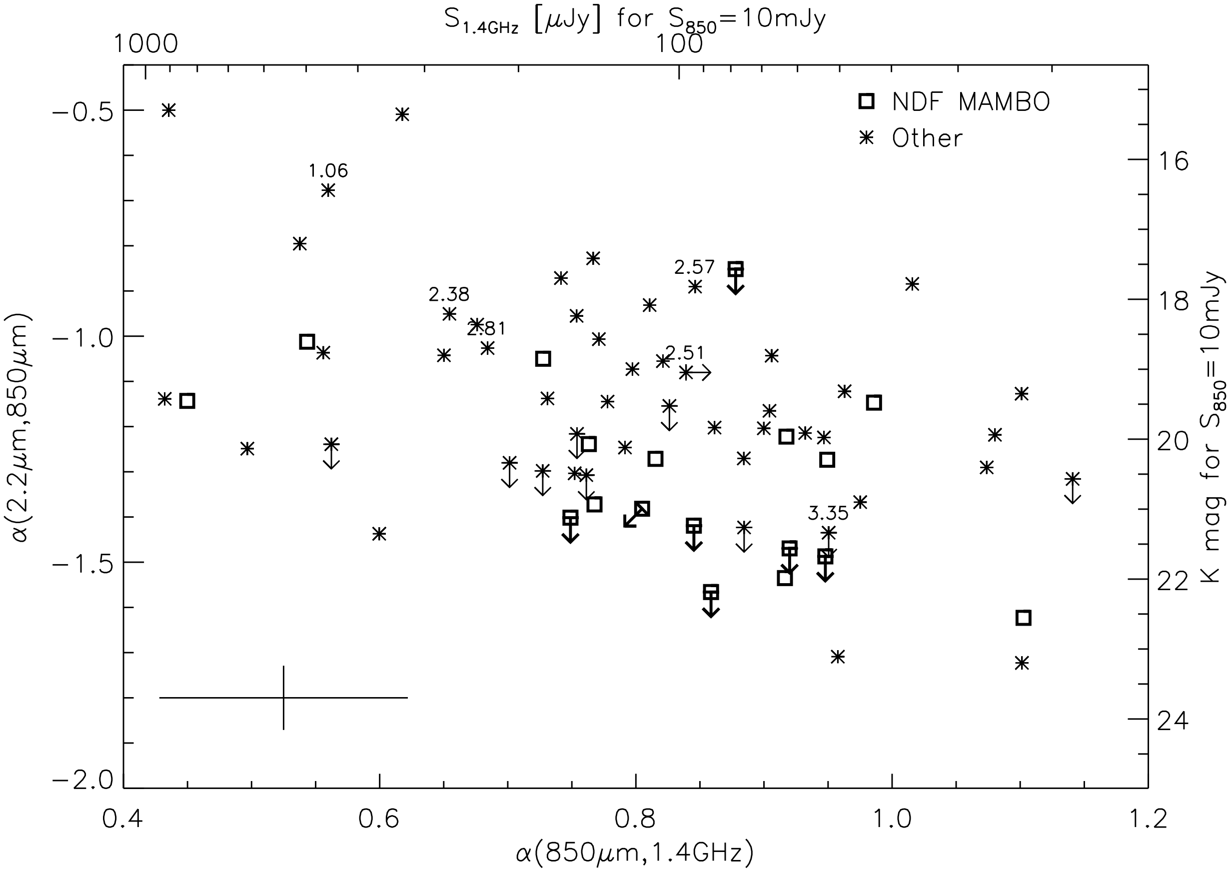
S1.4GHz [μJy] for S850=10mJy
1000
100
NDF MAMBO
Other
1.06
2.38
2.81
2.57
2.51
3.35
α(2.2μm,850μm)
K mag for S850=10mJy
α(850μm,1.4GHz)

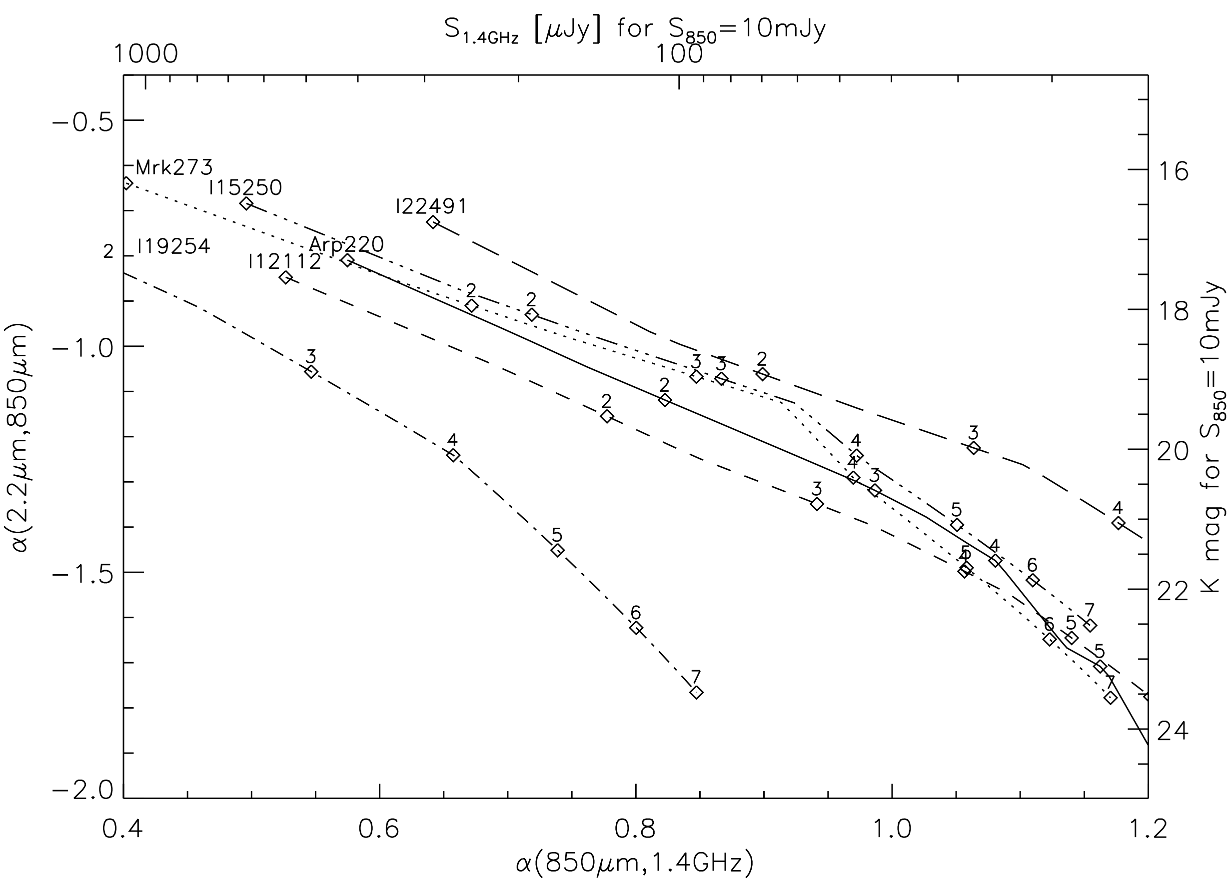
S1.4GHz [μJy] for S850=10mJy
1000
100
Mrk273
I15250
I22491
I19254
Arp220
I12112
α(2.2μm,850μm)
K mag for S850=10mJy
α(850μm,1.4GHz)